Chapter 5

Confined growth of $NiCo_2S_4$ on 2D/2D porous carbon self-repairing g-C_3N_4/rGO heterostructure for enhanced performance of asymmetric supercapacitors

Contents

5.1. Introduction

In recent decades, growing environmental pollution and global warming have led to the usage of renewable energy sources, with many researchers focusing on the associated energy storage and conversion systems [1-3]. Electrochemical capacitors or supercapacitors have gained great attention among energy storage technologies owing to their superior specific capacitance, high power density, energy density, cycling stability, etc. [4]. Supercapacitors (SCs) are primarily categorised as electrical double layer capacitors (EDLC) and pseudocapacitors subject to their energy storage method [5]. In EDLCs, charge storage is caused by the reversible adsorption or desorption of electrolyte ions at the electrode surface, whereas in pseudocapacitors, energy storage is caused by the rapid and reversible Faradaic redox processes [6]. Carbon and carbon derived materials shows EDLC behaviour while transition metal oxides (TMOs) and conducting polymers (CPs) shows pseudocapacitive properties. Comparatively, pseudocapacitive materials have higher charge storage properties. However, direct application of pseudocapacitive materials are limited due to its lower electrochemical stability and power density, as diffusion of electrolyte ions controls the Faradaic charge transfer reactions in a significant manner [7].

This chapter discusses the synthesis of a novel carbon self-repairing g-C_3N_4/reduced graphene oxide heterostructure and its hybridisation with $NiCo_2S_4$. This chapter consists of two sections. In the initial part, a novel hierarchical porous N, S doped reduced graphene oxide- $NiCo_2S_4$ hybrid nanocomposite was developed. The materials are optimized by determining the proper ratio of metal ions to graphene in order to obtain optimal supercapacitive performance. In the second part, synthesis method for the confined growth of $NiCo_2S_4$ on 2D/2D porous carbon self-repairing g-C_3N_4/rGO heterostructure as hybrid material for supercapacitor electrodes is discussed. The electrochemical activity is enhanced by the synergistic action of rGO with a large surface area and extended highly reactive region and defects in pCCN which facilitated the nucleation and confined growth of $NiCo_2S_4$ in the framework.

5.2. Synthesis and optimization of N, S doped Reduced Graphene Oxide-$NiCo_2S_4$ hybrid active material for all-solid-state asymmetric supercapacitor

Graphene, a 2D carbon allotrope, and its derivatives, graphene oxide (GO) and reduced graphene oxide (rGO), are the most desirable EDLC materials for energy storage applications because of their enormous surface area, large specific capacitance, high mechanical strength, and strong cycle stability, etc. [8]. The introduction of rGO will provide an abundance of active locations for metal ions development owing to its higher specific surface area. Moreover, the in-situ growth of $NiCo_2S_4$ over the rGO structure will prevent the structural collapse because of the volume fluctuation throughout the charging/discharging operation [9]. The higher conductivity of rGO when composited with intrinsically lower conducting $NiCo_2S_4$ will improve the electrochemical performance and at high current densities it alleviates the sluggish pace of redox reaction [10]. Nevertheless, an excessive quantity of graphene will create its own agglomeration, which will severely reduce graphene's utilisation efficiency and inhibit the formation of metal ions on its surface. In addition, the capacitance contribution is minimal in the working voltage range of $NiCo_2S_4$ electrodes (0 to 0.6 V) [11, 12], implying additional mass of graphene would obviously decrease the device's overall specific capacitance [13]. Also, non-homogeneous $NiCo_2S_4$ particle dispersion on graphene surface, absence of pores necessary for fast ionic transfers, self-aggregation along with restacking of graphene, etc. are also some other issues associated with $NiCo_2S_4$ -graphene composites. So, it is crucial to optimise the material by determining the proper ratio of metal ions to graphene in order to attain the best supercapacitive performance.

Here, utilising a simple hydrothermal technique, a new hierarchical porous N, S doped reduced graphene oxide—$NiCo_2S_4$ was synthesized by in situ growth of $NiCo_2S_4$ into a porous rGO structure. Ni^{2+} and Co^{2+} (metal ions) development over rGO promotes active sites for enhanced electrochemical activity, and the rGO framework concurrently improves ion transportation and electron conduction. The optimal utilisation of materials resulted in enhanced nucleation and confined growth of $NiCo_2S_4$ over rGO by taking benefit of rGO's larger surface area and porosity. The optimal proportion of materials were identified by synthesising samples at different ratios and evaluating its electrochemical performances. The prepared GNCS3 electrode displayed exceptional specific capacitance of 1640 F/g (1A/g). The overall electrochemical analysis suggests that GNCS3 is an ideal material for supercapacitor applications.

Experimental section

Materials required

Graphite flakes, Nitric Acid (70%), Sulfuric acid (98%), Potassium Permanganate, Hydrochloric acid (30%), Hydrogen Peroxide (30%), Nickel nitrate hexahydrate, Cobalt nitrate hexahydrate, Na_2S, Urea, were procured from Merck and Sigma-Aldrich. All chemicals were of analytical grade and there was no purification or processing of any of the chemicals before usage

Material Characterization

Fourier Transform Infrared spectroscopy (FTIR) was performed in Nicolet Impact 410 FTIR spectrophotometer. Powder X-ray diffraction (XRD) were conducted using Bruker AXS D8FOCUS (Cu-Ka radiation, k = 1.540598 A, 30 kV, 15 mA, scan rate of 1°/min). Raman spectra were obtained using Renishaw basis series with 514 lasers. Thermo Scientific UV-10 Spectrometer was utilized for performing UV–Vis spectroscopy at room temperature. Transmission Electron Microscopic (TEM) analysis was carried out in TECNAI G2 20 S-TWIN (200 kV) to investigate the morphology.

Electrochemical measurement

The $NiCo_2S_4$/rGO and $NiCo_2S_4$ nanostructures' electrochemical characteristics were investigated on a three-electrode setup using Autolab PGSTAT128 Potentiostat/Galvanostat Electrochemical workstation. The experiments were conducted at room temperature using Platinum electrode (counter electrode), Ag/AgCl (reference electrode) and 3M KOH electrolyte solution. The working electrodes were developed by mixing 90 wt% active materials, 10 wt% acetylene black and Nafion binder in N-methyl-2-pyrrolidone solvent, stirred for around 2h to create a slurry. The stainless steel substrate (surface area 1 cm^2) was subsequently coated with the slurry, which was then dried overnight (80 °C) in a vacuum oven. CV, GCD and EIS were used to analyse the as-prepared materials' electrochemical characteristics.

Fabrication of asymmetric supercapacitor

The 2-electrode device was fabricated with GNCS3 as anode, AC as cathode material along with PVA/KOH gel electrolyte. The mass ratio of anode to cathode was calculated to be 1:3 according to the eq.:

$$\frac{m_+}{m_-} = \frac{C_{s-} * \Delta V_-}{C_{s+} * \Delta V_+} \quad \ldots\ldots\ldots\ldots (1)$$

where, $m_+$and m_- denote masses, C_{s_+} and C_{s_-} are the specific capacitances, $\Delta V_+$and ΔV_- are the potential windows of the anode and cathode respectively.

Preparation of $NiCo_2S_4$/rGO nanocomposite

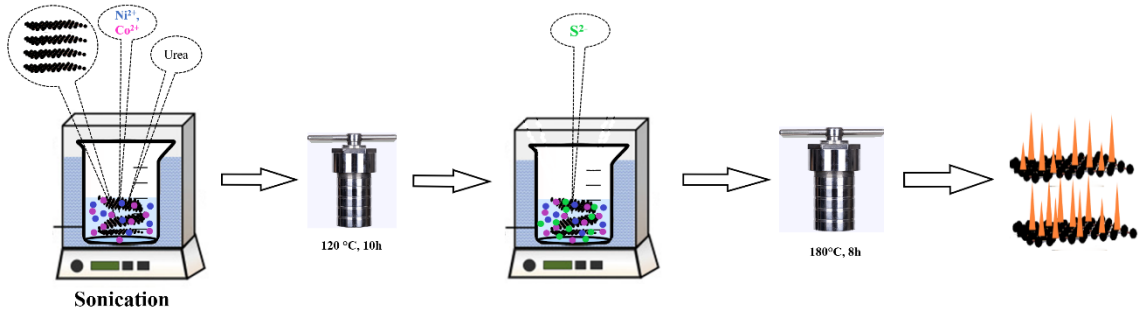

Fig.5.1. Schematic diagram for the synthesis of N,S doped rGO/$NiCo_2S_4$

GO was synthesised by oxidizing graphite flakes employing a modified version of the Hummers process [14]. In a typical procedure, 20 mg of GO powder was sonicated for one hour in 40mL of DI water to obtain a homogeneous solution of GO (Fig.5.1). A specified quantity of $Ni(NO_3)_2{\cdot}6H_2O$, $Co(NO_3)_2{\cdot}6H_2O$ and urea (molar ratio of 1:2:10) were put into the GO solution during sonication. The solution was then kept in an autoclave and heated for 10 h at 120 °C. The rGO/NiCo-carbonate hydroxide (labelled as GNC) precursor formed was filtered and washed numerous times. The precursor was dispersed in 40 ml DI water with 600 mg of Na_2S and autoclaved at 180°C (8h). The finished black product so obtained was filtered, rinsed to pH neutrality, dried (70 °C) and was ready for use. The samples synthesised using 2mM, 4mM, 6mM, and 8mM of $Ni(NO_3)_2.6H_2O$ were designated as GNCS1, GNCS2, GNCS3, and GNCS4, respectively. For comparative purpose, bare $NiCo_2S_4$ was also synthesised using the same procedure without the addition of GO and was named as NCS.

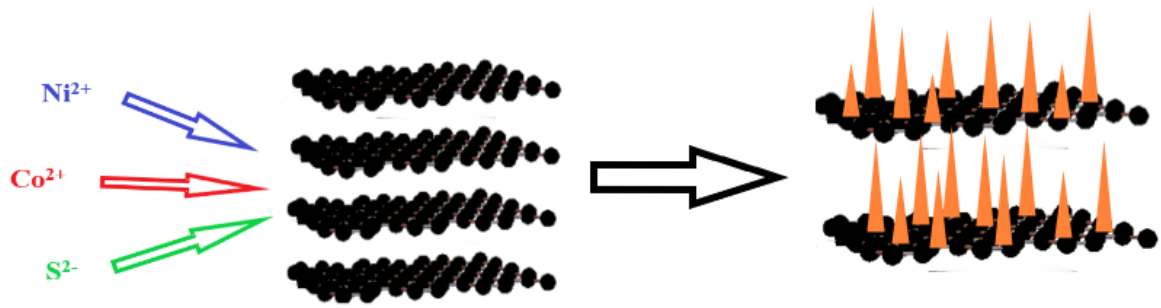

Fig.5.2. Schematic diagram of N, S doped rGO/$NiCo_2S_4$

Results and discussions

Material synthesis

Hydrothermal synthesis route was to prepare a novel hierarchical porous $NiCo_2S_4$/rGO nanocomposite material (Fig.5.2). Initially a homogenous solution of GO was prepared by ultrasonication. GO sheets were strongly negatively charged when dispersed in water owing to the ionisation of hydroxyl, carboxylic and phenolic groups on edges and surfaces [15]. The addition of $Ni(NO_3)_2$ and $Co(NO_3)_2$ into the GO solution caused electrostatic interaction between positively charged ions (metal ions) and the negatively charged ions (oxygen-containing groups) leading to the adhering of Ni^{2+} and Co^{2+} ions onto the GO nanosheet's surface [16]. The hydrolysis of Ni^{2+} and Co^{2+} ions resulted in formation of nickel cobalt hydroxide as an intermediate product. As a sulfur source, Sodium Sulfide was added and the resultant solution was autoclaved at 180 ºC for 8h to transform the intermediate into $NiCo_2S_4$. Finally, N, S dual doped $NiCo_2S_4$/rGO hybrid with $NiCo_2S_4$ nanoneedles evenly attached on rGO sheets was achieved.

Structural and morphological characterisation of $NiCo_2S_4$/rGO

The FTIR spectrum of GO and $NiCo_2S_4$/rGO nanocomposites is shown in Fig.5.3a. The hydroxyl group (-OH) and residual water molecules' stretching vibrations are responsible for the broad peak at 3410 cm^{-1} in the FTIR spectra of GO [14]. The absorption peaks at 1720 cm^{-1} (C=O stretching), 1620 cm^{-1} (C=C; skeletal vibration from sp2 carbon rings) and 1150 cm^{-1} (C–O–C groups) further confirms the existence of oxygen functionalities in the sample [17]. However, the oxygen functionalities found in GO were significantly reduced in the spectrum of $NiCo_2S_4$/rGO confirming the successful reduction of GO [18].

XRD analysis was done to characterise the phase difference in samples (Fig.5.3b). The GO's spectra show a diffraction peak at 2θ=9.92º, attributing to the reflection of (002) plane of GO [19]. It can be seen that the XRD spectra of $NiCo_2S_4$/rGO and $NiCo_2S_4$ are identical. The peaks at 2θ values of 16.2º, 26.6º, 31.4º, 38.1º, 50.32º and 55.16º corresponds to the (111), (220), (311), (400), (511) and (440) reflections of cubic phase $NiCo_2S_4$ (JCPDS 20-0782) respectively. Also, (001) peak of GO at 2θ=9.92º disappeared indicating the complete exfoliation/reduction of GO into rGO. Additional peaks were found at 29.76º and 52.42º for NCS sample which corresponds to the (311) and (440) lattice planes of face centred cubic Co_9S_8 (JCPDS 65-6801) [10]. The formation of these two phases were not anticipated. The peaks attributed to Co_9S_8 are significantly diminished after nanocompositing with rGO,

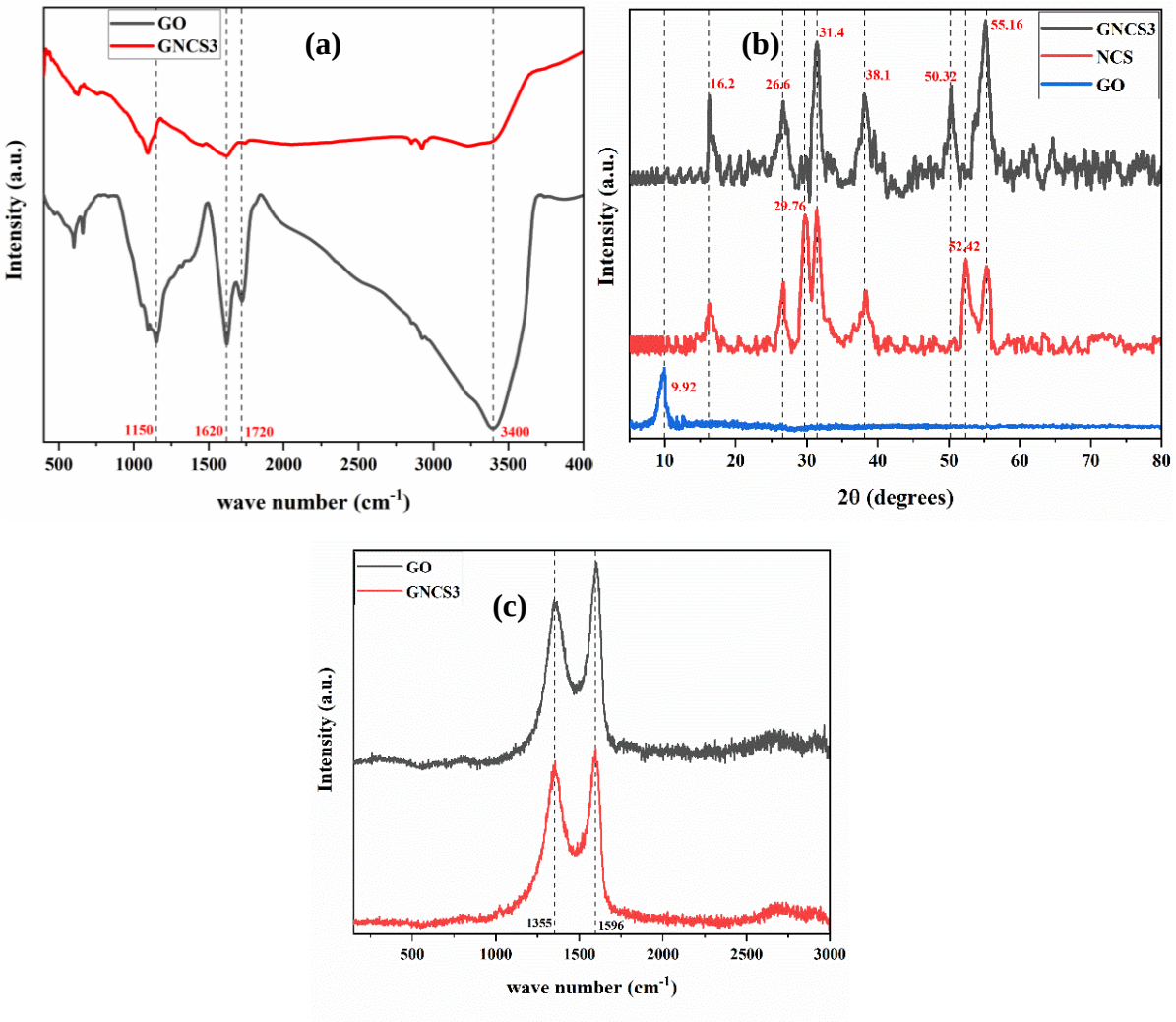

Fig.5.3 (a) FTIR spectra of GO and GNCS3 (b) XRD spectra of GO, NCS and GNCS3 (c) Raman spectra of GO and GNCS3

indicating the effectiveness of graphene in reducing multiphase crystallisation during crystal formation in the material. Since no other diffraction peaks were found, it can be concluded that pure phase $NiCo_2S_4$ was synthesized and that the GO's presence had no impact on the material's crystalline structure.

Raman spectroscopic analysis was carried out to characterize disorder and defects in the graphitic structure. Fig.5.3c shows the Raman spectra of GO and GNCS3 nanocomposites. The D and G bands are distinctly seen in the Raman spectra of both samples. The G band, centred at 1596 cm^{-1}, is a consequence of stretching vibrations in the basal plane of graphene and is commonly caused by E2g phonon of C sp2 atoms. The structural deformities and disorders are reflected in the frequency range of the D band (1355 cm^{-1}) and is generated by a breathing k-point phonon with A1g symmetry [20]. The intensity ratio D to G band (I_D/I_G) implies the

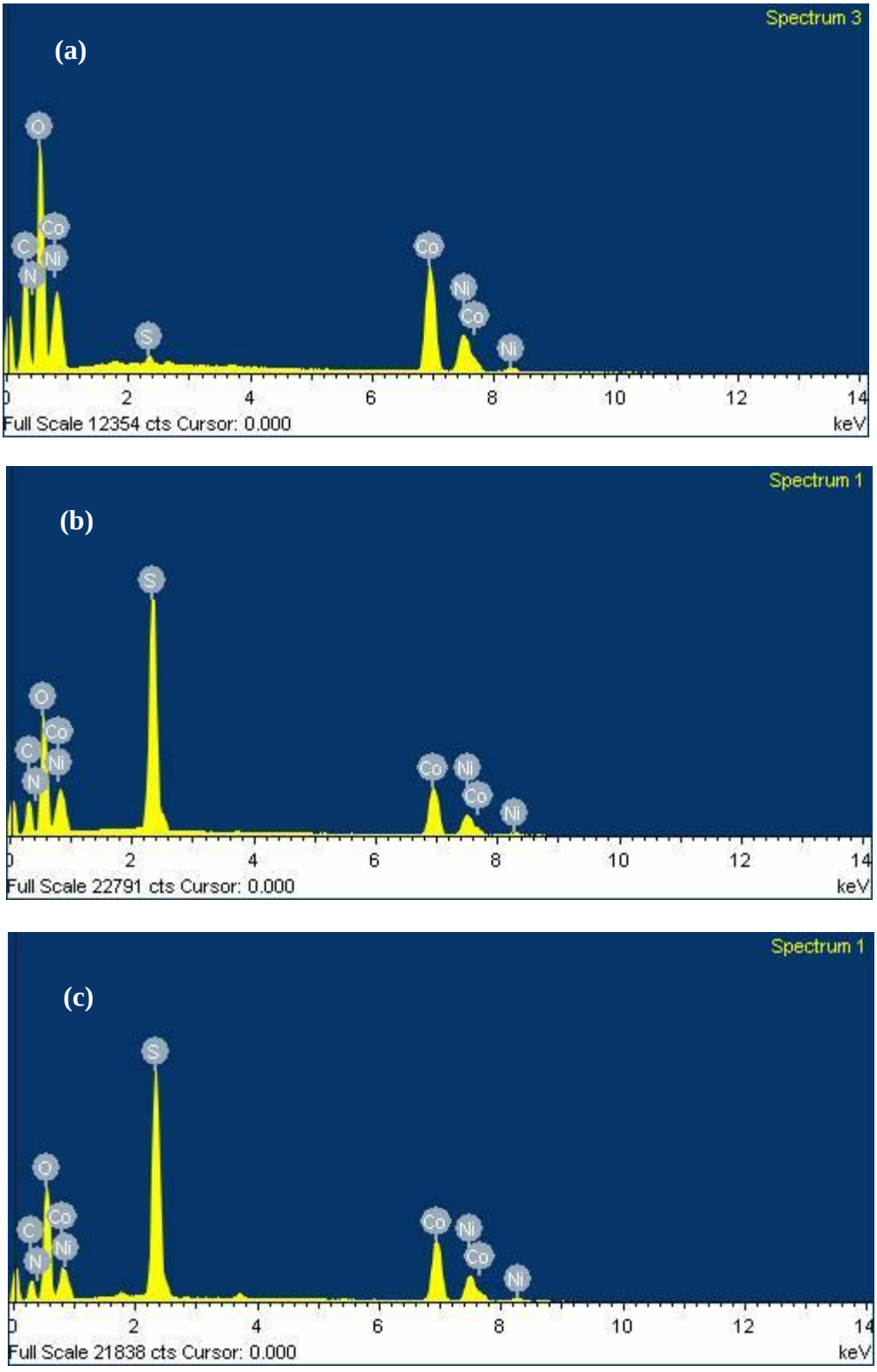

Fig.5.4 (a) EDS spectra of $NiCo_2OH$. (b) EDS spectra of $NiCo_2S_4$. (c) EDS spectra of rGO/$NiCo_2S_4$.

Elemental composition of $NiCo_2OH$		
Element	Weight%	Atomic%
C K	25.92	40.03
N K	2.76	3.65
O K	39.93	46.31
S K	0.43	0.25
Co K	21.80	6.86
Ni K	9.16	2.90
Totals	100.00	

Elemental composition of $NiCo_2S_4$		
Element	Weight%	Atomic%
C K	24.86	39.12
N K	1.28	1.72
O K	36.30	42.87
S K	15.75	9.29
Co K	14.72	4.72
Ni K	7.09	2.28
Totals	100.00	

Elemental composition of $rGO/NiCo_2S_4$		
Element	Weight%	Atomic%
C K	17.69	30.12
N K	3.77	5.50
O K	34.76	44.42
S K	16.38	10.45
Co K	18.59	6.45
Ni K	8.80	3.06
Totals	100.00	

Table.5.1 Elemental composition of $NiCo_2OH$, $NiCo_2S_4$ and $rGO/NiCo_2S_4$

structural defects and disorders in the graphitic structures [21]. The I_D/I_G value increased from 0.84 for GO to 0.94 for GNCS3, indicating disorder induced by the heteroatom doping in the graphene structure and the existence of more tiny, isolated sp2 graphene domains in GNCS3 [14, 22, 23].

EDS spectrum of NC, NCS and GNCS3 is shown in Fig.5.4. The initial Ni to Co molar ratio used in the synthesis of GNCS3 is in agreement with the observed atomic ratio of Ni to Co, which is around 1:2. For NCS, the amount of Co is slightly higher than the expected ratio of 1:2 (Ni:Co) owing to the formation of Co_9S_8 crystals which is compatible with the XRD results. Compared to NCS, GNCS3 has a greater S and N content as a result of co-doping of S and N into the rGO lattice. The chemical doping of N and S atoms alters the uniformity and introduces numerous defects in the crystal structure by replacing the lattice C atoms thereby rendering the graphene structure more disordered [24, 25].

The surface area and pore size distribution of GNCS3 sample were studied employing the Brunauer - Emmett - Teller (BET) analysis. The N_2 adsorption–desorption isotherm (Fig.5.5) exhibits type IV isotherm characteristics with an H3 hysteresis loop, suggesting the presence of mesoporous structure [26]. The surface area of the GNCS3 sample was calculated to be 254.18 m^2/g. The high surface area of the material is due to the optimum use of materials which inhibited the agglomeration of ingredients. In addition, the wedging in of $NiCo_2S_4$ nanoneedles in between the graphene layers further aided in the formation of few layers graphene with high surface area. The pore size distribution of 2.94-25.01nm confirms the mesoporous structure of the sample in addition to some macropores. The GNCS3 sample showed high pore volume of

0.63cc/g. The porous structure and high pore volume of GNCS3 sample offers more active sites for electrochemical reactions, hence enhancing the material's supercapacitor performance [27, 28].

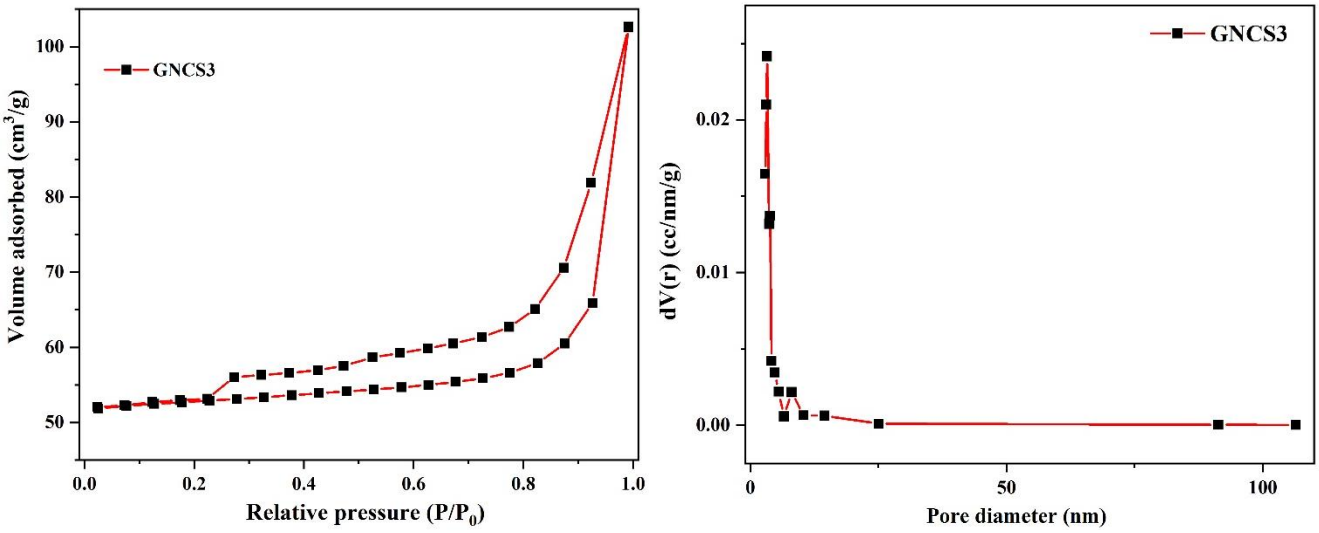

Fig.5.5 (a) N_2 adsoprtion-desorption isotherm of GNCS3. (b) Pore size distribution of GNCS3

TEM imaging was used to characterise the morphology of the as-synthesized GNCS3 samples (Fig.5.6(a-c)). The sheet like morphology of highly transparent, atomic thin rGO nanosheets was evident in the TEM images [14]. The rGO sheets are transparent, with plainly visible wrinkles and curled edges implied that the achieved rGO primarily comprised of single or few graphene layers [29]. The imaging results further reveals that the GNCS3 sample consist of $NiCo_2S_4$ nanoneedles grown over rGO structure. The nanoneedles are evenly covered by rGO providing high specific surface area to the sample. The SAED pattern of GNCS3 confirms the polycrystallinity of the sample and the diffraction rings can be indexed to (111), (311), (511) and (440) planes of cubic phase $NiCo_2S_4$ which supports the XRD results [30].

Electrochemical analysis of $NiCo_2S_4$ and rGO/$NiCo_2S_4$ at different molarities

The cyclic-voltammogram (CV) of all samples at 20mV/s of scan rate is depicted in Fig.5.7a. The shapes of CV plots show the pseudocapacitive behaviour of the materials and also the shape doesn't changes even after the addition of rGO which implies the nanocompositing of rGO doesn't affect the energy storage mechanism of the metal sulphide material. The active material-electrolyte ions interaction results in two evident redox peaks as [10]:

$$NiCo_2S_4 + 2OH^- \longleftrightarrow NiS_{2x}OH + Co_2S_{4-2x}OH + 2e^- \quad \text{..... (1)}$$

$$Co_2S_{4-2x}OH + 2OH^- \longleftrightarrow 2CoS_{2-x}O + 2H_2O + 3e^- \quad \text{..... (2)}$$

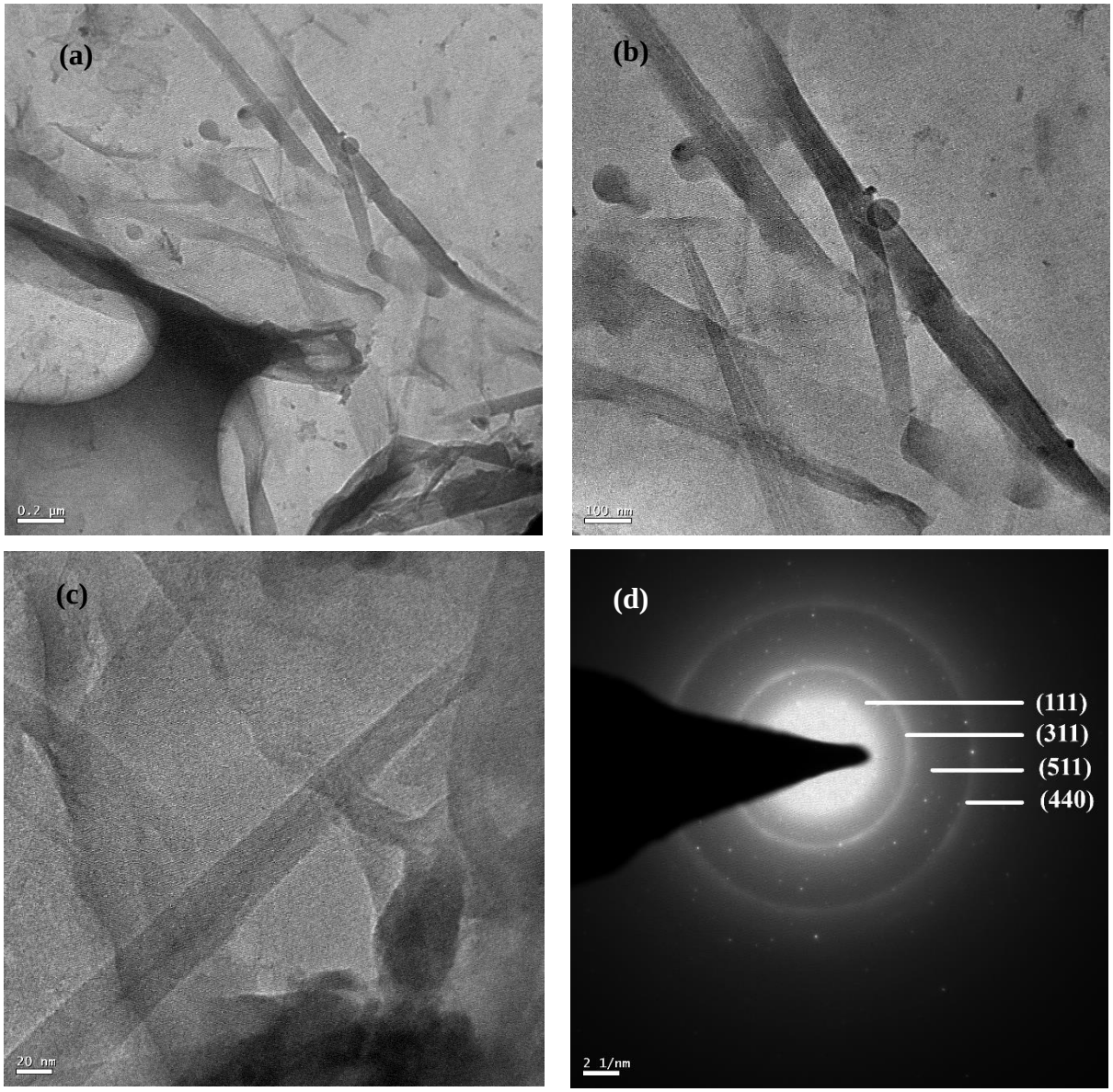

Fig.5.6. (a-c) TEM images of GNCS3 (d) SAED pattern

The magnitude of area enclosed in the CV curve is GNCS3>NCS>GNCS2>GNCS4>GNCS1. The CV curve of GNCS3 (Fig.5.7a) exhibited the highest current density compared to other samples, showing a substantially enhanced electrochemical capacitance because of the optimal ratio of rGO to $NiCo_2S_4$. The optimal concentration of $NiCo_2S_4$ utilised prevented the aggregation of graphene layers during the restacking process, which contributed to the enhancement of electrochemical performance. The $NiCo_2S_4$ nanoneedles were wedged-in between the graphene layers while the nucleation of $NiCo_2S_4$ in the solution to form graphene with very few layers while restacking. Electrochemical performance is improved as a result of the creation of few-layer graphene due to its increased conductivity and surface area [31]. As

with GNCS4, excessive use of $NiCo_2S_4$ leads to agglomeration, which may raise electrode resistance and decrease reaction kinetics, resulting in decreased capacitance. In addition, the over utilization of rGO may result in the same issue as in GNCS1 due to the aggregation of graphene layers. Fig.5.7b depicts the CV plots of GNCS3 at various scanning rates. The area of CV curve increased with increasing scan rates as expected.

The following equation describes how quantitative analysis is used to analyse the charge storage kinetics of GNCS3 in further detail [32]:

$$i = a\vartheta^b \quad \ldots\ldots\ldots\ldots\ldots\ldots\ldots (3)$$

$$\log(i)=\log(a)+b\log(\vartheta) \quad \ldots\ldots\ldots (4)$$

where, i=peak current (A), ϑ=scan rate (mV/s) and b=constant. From eq.(4), b is the slope of the linear equation. The energy storage mechanism is surface controlled (capacitive process) for b=1 and is diffusion controlled (pseudocapacitive process) for b=$\frac{1}{2}$. When $\frac{1}{2} < b < 1$, the process is cumulative impact of capacitive and pseudocapacitive process. Fig.5.7c shows the linear relationship of log(peak current) and log(scan rate). After linear fitting, the plot's slope is b=0.788, implying that the kinetics of charge storage is the cumulative effect of surface controlled as well as diffusion controlled process. Trasatti method was employed to identify the capacitance contribution due to Electron Double Layer (EDL) Capacitance and Pseudocapacitive effect. The gravimetric capacitance was analysed for various scan rates using the eq [33, 34]:

$$C_s = \frac{A}{2*\vartheta*V} \ldots\ldots\ldots\ldots\ldots\ldots (5)$$

where, C_s= gravimetric capacitance(F/g), A=area under the CV curve, ϑ=scan rate(V/s) and V=potential window(V). Assuming semi-infinite diffusion of ions (i.e., ions unrestrictedly diffuse to electrode/electrolyte interface from bulk electrolyte), the relationship in C^{-1} vs $\vartheta^{\frac{1}{2}}$ plot will be linear and the fitted line's intercept will give the reciprocal of total capacitance (C_t).

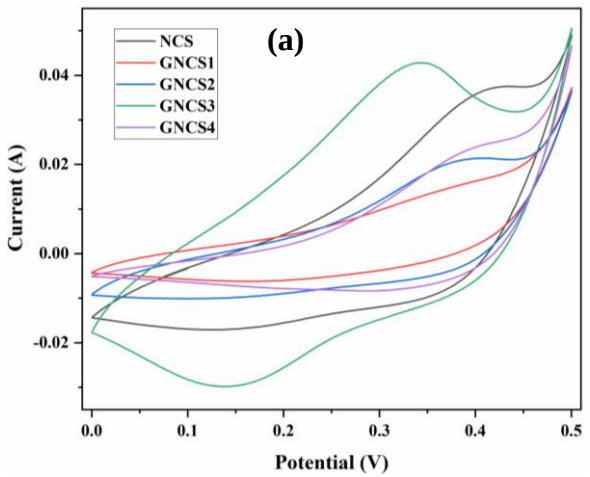
(a)
NCS
GNCS1
GNCS2
GNCS3
GNCS4
Current (A)
Potential (V)

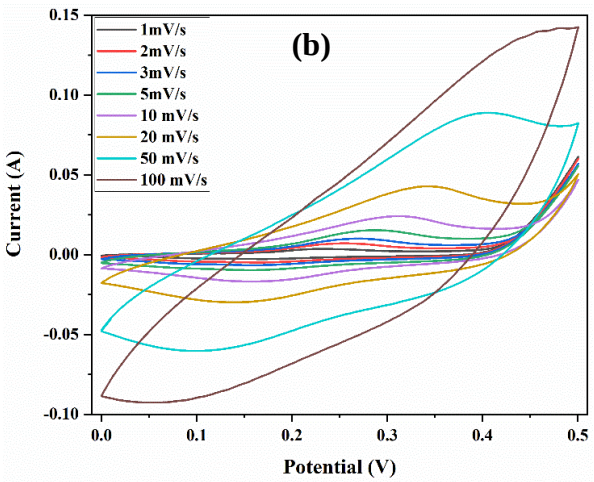
(b)
1mV/s
2mV/s
3mV/s
5mV/s
10 mV/s
20 mV/s
50 mV/s
100 mV/s
Current (A)
Potential (V)

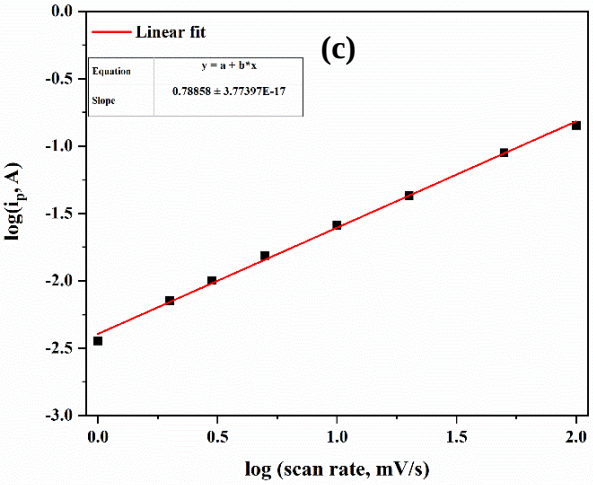
(c)
Linear fit
Equation
y = a + b*x
Slope
0.78858 ± 3.77397E-17
log(i_p, A)
log (scan rate, mV/s)

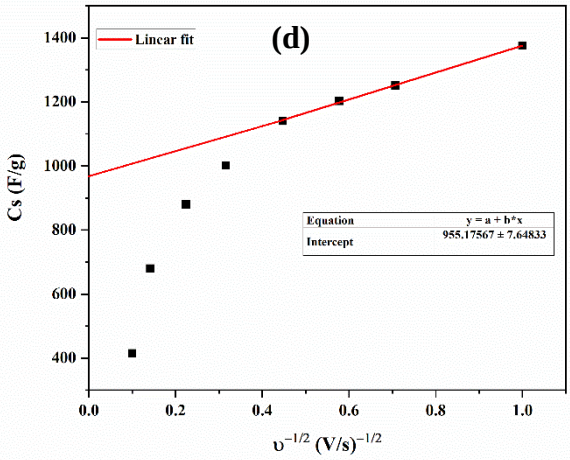
(d)
Linear fit
Equation
y = a + b*x
Intercept
955.17567 ± 7.64833
Cs (F/g)
υ^-1/2 (V/s)^-1/2

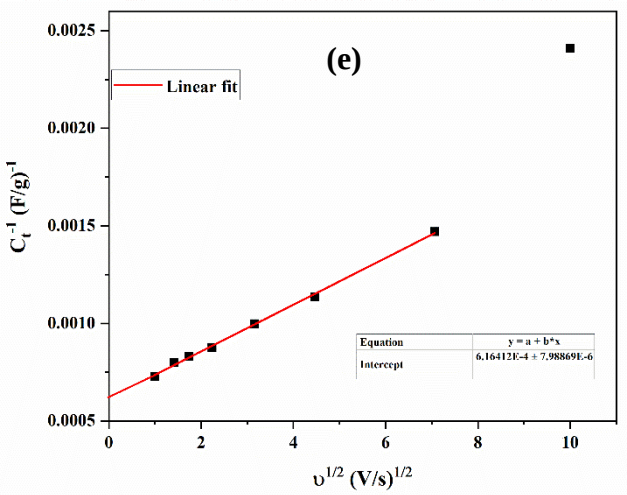
(e)
Linear fit
Equation
y = a + b*x
Intercept
6.16412E-4 ± 7.98869E-6
C_t^-1 (F/g)^-1
υ^1/2 (V/s)^1/2

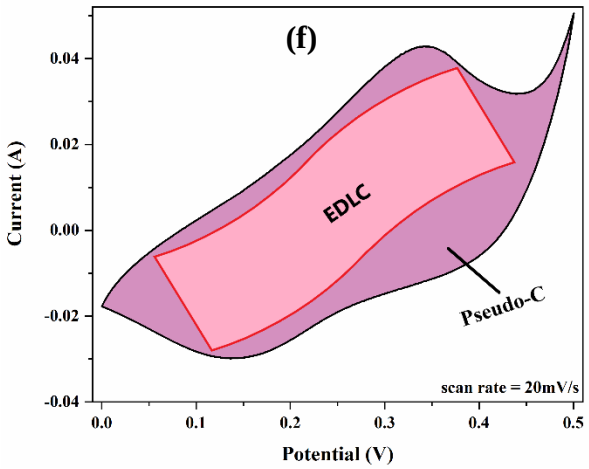
(f)
EDLC
Pseudo-C
scan rate = 20mV/s
Current (A)
Potential (V)

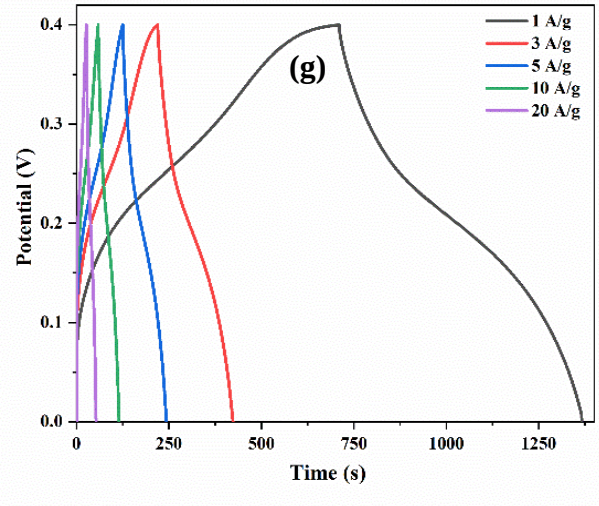
(g)
1 A/g
3 A/g
5 A/g
10 A/g
20 A/g
Potential (V)
Time (s)

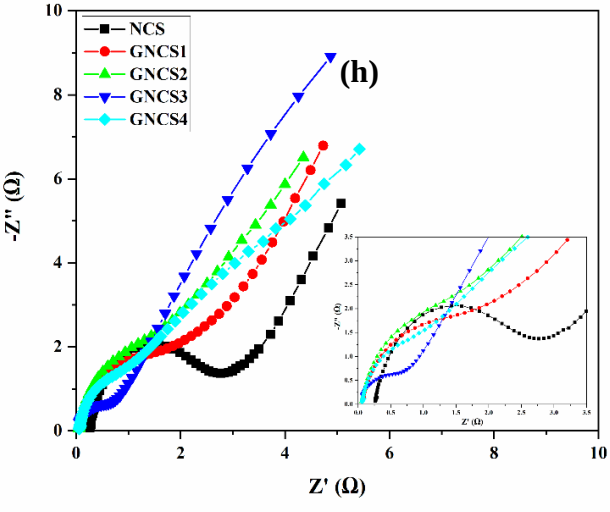
(h)
NCS
GNCS1
GNCS2
GNCS3
GNCS4
-Z'' (Ω)
Z' (Ω)

Fig.5.7. (a) CV curves of NCS, GNCS1, GNCS2, GNCS3 and GNCS4 at 20mV/s. (b) CV curves of GNCS3 at different scan rates. (c) Relationship between log(peak current) and log(scan rate). (d) Relationship between Specific capacitance and (scan rate)$^{-1}$. (e) Relationship between (Specific capacitance)$^{-1}$ and scan rate. (f) CV of GNCS3 at 20mV/s (g) GCD curves of GNCS3 at different current densities. (h) EIS curves of NCS, GNCS1, GNCS2, GNCS3 and GNCS4.

The electrode's inherent resistance and deviation from semi-infinite ion diffusion resulted in variation from the linear relationship of the data points collected at greater scan rates. During linear fitting, these erroneous data points were suppressed. The relationship can be described as in eq. [34]:

$$C_s^{-1} = constant * \vartheta^{\frac{1}{2}} + C_t^{-1} \text{.... (6)}$$

where, $C_t = C_{pseudo} + C_{EDL}$..... (7)

Under the same assumption of semi-infinite diffusion of ions, the plot between gravimetric capacitance and $\vartheta^{-\frac{1}{2}}$ will also give a linear relationship and the y-intercept of the fitted line will give EDL capacitance (C_{EDL}). So, from eq. (7),

$$C_{pseudo} = C_t - C_{EDL} \text{ ..... (8)}$$

The capacitance contribution can be found out by following eq:

$$C_{EDL}\% = \frac{C_{EDL}}{C_t} * 100\% \text{ ..... (9)}$$

$$C_{pseudo}\% = \frac{C_{pseudo}}{C_t} * 100\% \text{.....(10)}$$

From fig.5.7d, C_{EDL}=955F/g is the contribution of EDL capacitance and from fig.5.7e, the inverse of y-intercept gives the total capacitance, C_t=1622F/g. From eq. (8), C_{pseudo} =667F/g. From eq. (9) and (10), $C_{EDL}\% = 58.88\%$ and $C_{pseudo}\% = 41.12\%$ [Fig.5.7f].

Fig.5.7g displays the GCD curve of GNCS3 at varied current densities. The below mentioned equation was used for computation of specific capacitances from GCD curves:

$$\text{Specific Capacitance, } C_s = \frac{I.\Delta t}{m.\Delta V} \text{ F/g}$$

where, I = charge/discharge current (A), Δt = discharge time (s), m = mass of the active material of the electrode (g), and V = potential window (V). The capacitance value of GNCS3 at current densities 1A/g, 3A/g, 5A/g, 10A/g and 20A/g are 1640F/g, 1523F/g, 1475F/g, 1400F/g and 1305F/g respectively. As seen, at increasing current densities the specific capacitance drops

progressively, which may be attributed to the iR drop and the inability of ions to permeate the electrode surface for redox reactions at higher current densities [35].

The reaction kinetics of the electrodes were evaluated using Electrochemical Impedance Spectroscopy (EIS). All EIS curves [Fig.5.7h] had a similar semi-circular shape and sloped line shape. In the low frequency range, the slope of the line reflects the Warburg resistance caused by ion diffusion from the electrolyte to the surface of the electrode. The most vertical line of GNCS3 compared to other samples implies that GNCS3 showed a much faster ion transport with lowest diffusion resistance, which are ideal behaviour for supercapacitors. This may be owing to the sample's rGO layers' porous nature and large surface area, which facilitate the easier penetration of ions into its surface. Additionally, the low bulk resistance and fast response kinetics of GNCS3 are further suggested by the smaller diameter of the semicircle and the lowest x-intercept at the beginning of the semicircle [36]. This is because of the highly conductive nature of very few layer graphene nanosheets which acts as a conducting framework for the fast transport of electrons [37]. These results suggest that GNCS3 has high charge-transfer capacity, rapid redox reactions as well a better structural strength. The overall electrochemical analysis implies that GNCS3 is an ideal material for supercapacitor applications.

An asymmetric supercapacitor (ASC) was fabricated and its electrochemical performance was evaluated for assessing the practical applications. The CV curves of GNCS3//AC ASC (Fig.5.8a) are scanned from 1 to 100mV/s. The deviation of the CV curve from a rectangular form and the existence of redox peaks indicates the pseudocapacitive nature of the device. Also, the similar shape of the curve at varying scan rates implies the excellent fast-charge/discharge behavior of the device. Fig.5.8b shows the GCD curve of GNCS3//AC ASC at various current densities from 1A/g to 20A/g and showed best calculated specific capacitance of 135F/g at 1A/g. Similarly, specific capacitance of 120F/g, 116F/g, 108F/g and 100F/g was calculated for current densities 3A/g, 5A/g, 10A/g and 20A/g respectively. The intrinsic resistance of the electrode and incomplete faradaic redox reactions at greater current densities cause decrease in specific capacitance with increasing current density [38]. The cycling stability of GNCS3//AC ASC was studied by performing GCD at 10A/g for 5000 cycles. The device showed a capacitance retention of 92.5% after 5000 cycles as illustrated in fig.5.8c. Also, the inset shows first and last 10 GCD cycles and also first and 5000^{th} GCD wave of stability test.

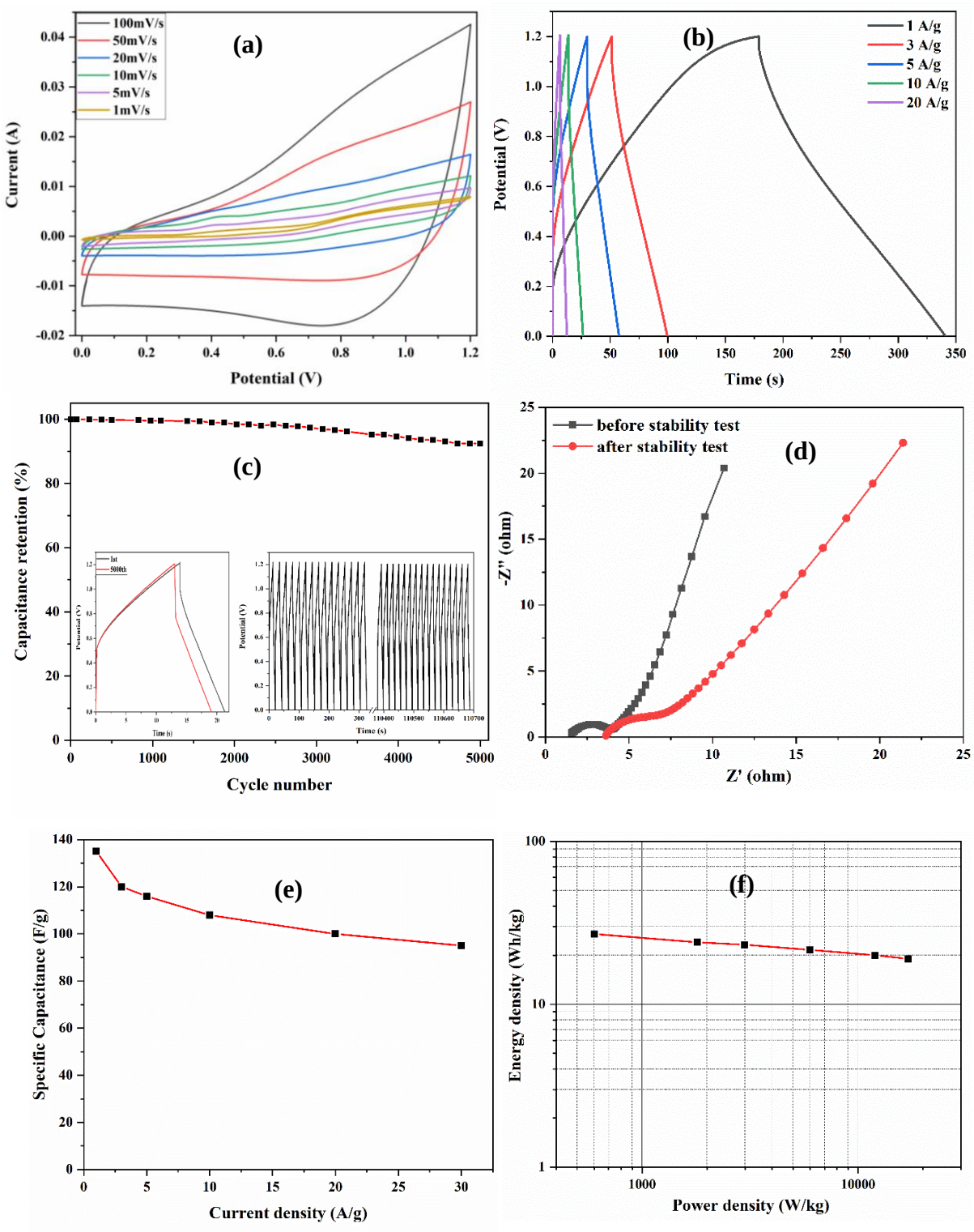

Fig. 5.8. (a) CV of GNCS3//AC at different scan rates (b) GCD of GNCS3//AC at different current densities (c) Capacitance retention of GNCS3//AC after 5000 cycles at 10 A/g. inset: initial and final GCD curve after 5000 cycles and first and last 15 cycles (d) EIS spectra of GNCS3//AC before and after cycling stability test (e) Specific capacitance of GNCS3//AC at different current densities (f) Power density Vs. Energy density plot of GNCS3//AC

The better cycling stability is due to the presence of few layer graphene and strong anchoring of $NiCo_2S_4$ nanoneedles to rGO nanolayers which prevents the volume change of $NiCo_2S_4$ during charge/discharge process [36, 39]. Even then, the decline in capacitance can be due to the following reasons [37]: 1) The Ni-Co-S electrode may degrade into hydroxides or oxides after many reactions with the alkaline electrolyte. 2) The delamination of the electrode material from the substrate after continuous charge/discharge process. 3) The degradation in the morphology of rGO/$NiCo_2S_4$ structure after rigorous cycling tests. To examine the charge storage kinetics, EIS was conducted before and after stability test as shown in Fig.5.8d. The Rs value before and after stability test were found after fitting to be 1.60Ω and 3.63Ω respectively. Similarly, Rct before and after stability test was 2.60Ω and 5.17Ω respectively. The significant change after stability test in Rs and Rct values is due to the degradation caused after prolonged use due to the above mentioned reasons. In addition, the increasing Rct value and slope deviation in the low frequency area show that the device's conductivity and ionic diffusion capabilities have decreased since the stability test [40]. The specific capacitance Vs. current density plot (Fig.5.8e) demonstrates that the device exhibits excellent stability with 70.4% specific capacitance even at 30A/g.

The energy density and power density are calculated using the eqs:

$$\text{Energy density, } E_s = \frac{C_s(V)^2}{2} * \frac{1}{3.6} \text{ Wh/kg}$$

$$\text{Power density, } P_s = \frac{E_s}{\Delta t} * 3600 \text{ W/kg}$$

where, Cs is the specific capacitance and V is the potential window. Fig.5.8f shows the power density Vs. Energy density plot of GNCS3//AC at different current densities. A maximum energy density of 27Wh/kg at power density of 600W/kg was obtained at a current density of 1A/g.

5.3. Confined growth of $NiCo_2S_4$ on 2D/2D porous carbon self-repairing g-C_3N_4/rGO heterostructure for enhanced performance of asymmetric supercapacitors

Due to increase in population, dependency on fossil fuel has increased unprecedently that eventually has led to huge negative impact on the environment. Need of the hour is to look for alternate renewable sources of energy to meet the perpetual demands of human race [3, 41, 42]. In present scenario, the importance of green energy such as wind, solar, tidal energies along with the devices to store such energies has tremendously escalated. Electrochemical capacitors (Supercapacitors) can play a huge role in this context due to higher cycling life and power density than batteries and fast charge/discharge rate [43]. However, the major hurdles in the development of supercapacitor are low energy density, narrow potential window and low conductivity of electrode materials [44]. And hence, creating new electrode materials with enhanced electrochemical properties is crucial for supercapacitors.

In the past years, graphitic Carbon Nitride (g-C_3N_4) has garnered much focus of researchers owing to their moderate bandgap, better chemical stability, interesting optical characteristics, etc. for photo-catalytic applications [45]. However, there aren't many studies that evaluate g-C_3N_4 (GCN) for use in energy storage applications. GCN has a structure resembling graphite with stacked 2D layers consisting of sp2 hybridized C and N atoms forming π-conjugated electronic structures [46]. Despite its high N content with C:N ratio of 3:4, the use of GCN in supercapacitors is restricted owing to their small surface area and poor conductivity [47]. Nanocompositing with graphene is found to be successful in improving the conductivity and electrochemical properties of GCN [48]. The abundant highly reactive region and defects in GCN serves as a framework for crystal nucleation and growth [49]. Chen and colleagues demonstrated that 3D-GCN functionalized graphene displayed a capacitance of 264F/g at 0.4A/g and excellent cycling stability [50]. Ding and co-workers reported a carbon self-repairing g-C_3N_4 (CCN) via homogeneous substitution of C instead of N or by creation of new interstitial C-N bonds. The CCN with extended π-conjugated layers formed porous framework through cross-linking interactions with rGO layers. As a result, CCN@rGO electrode presented a specific capacitance of 380F/g at 0.25A/g [48]. Later, Lin and co-workers report that the peroxidation of GCN in HNO_3 trims down the larger planes into smaller segments thereby increasing the edge nitrogen and oxygen functionalities. The GOOCN24 electrode material thus developed exhibited 266F/g and 244F/g at acid and alkali electrolytes respectively at 1A/g [51]. However, the energy density of GCN, graphene or their nanocomposites are low due to the predominant EDLC charge storage mechanism of the materials.

Recently, bimetallic sulfides receive much attention due to higher electrochemical activity than that of their oxides [52]. Among them, $NiCo_2S_4$ has reported to be a material of exceptional pseudocapacitive properties and high conductivity. Moreover, it has low bandgap and exhibit fast Faradaic redox reactions due to multiple valance transitions [53]. In this direction $NiCo_2S_4$ honeycomb/$NiCo_2S_4$ core-shell structure are found to have excellent areal capacitance of 17.56F/cm^2 at 5mA/cm^2 exhibiting 3 times greater areal capacitance than that without core-shell structure [54]. Ouyang and co-workers synthesised a porous $NiCo_2S_4$ nanosheets which showed a specific capacity of 1354C/g at 1A/g and excellent cycling stability of 82.5% at 10000 cycles [55]. The $NiCo_2S_4$ nanowires grown on carbon cloth with excellent areal capacitance of 1567mA/cm^2 at 1mA/cm^2 [56]. Mesoporous $NiCo_2S_4$ was reported by Zhu and co-workers which showed an remarkably high specific capacitance of 1440F/g at 3A/g with exceptional cycling stability [30]. However, direct application of $NiCo_2S_4$ are limited due to its lower electrochemical stability and power density [57]. To enhance the energy storage performances, hybrid electrode materials are developed by collaborating EDLC and pseudocapacitive materials to potentially explore the synergy between the components, which can deliver higher energy and power output with better stability [58]. Therefore, based on the foregoing, it is envisaged that the hybridization of $NiCo_2S_4$ with graphene and g-C_3N_4 will yield active nanomaterials having superior electrochemical characteristics for supercapacitors.

Here, we report a novel design and synthesis for confined growth of $NiCo_2S_4$ on porous carbon self-repairing g-C_3N_4/rGO heterostructure via a simple hydrothermal technique. The introduction of few layers graphene in the heterostructure increases the conductivity and surface area. The improved electronic conductivity and activity of carbon self-repairing g-C_3N_4 (CCN) than g-C_3N_4 is because of the creation of an extended delocalized π-electron by the substitutional or interstitial C atoms in the structure. Additionally, as a result of acid treatment, the larger planes of CCN are broken down into smaller segments, resulting in an increase in the edge nitrogen and oxygen functional groups. The incorporation of porous CCN resulted in a powerful electrostatic interaction with both GO and CCN, which assisted in the prevention of the aggregation of graphene sheets. The formation of porous carbon self-repairing g-C_3N_4/rGO heterostructure acted as a framework and backbone for the electron conduction and confined growth of $NiCo_2S_4$ within the framework. The hybrid material that was so synthesised showed good electrochemical characteristics in alkaline electrolytes, demonstrating that it is an attractive electrode material for supercapacitor applications.

Experimental section

Materials required

Graphite flakes, Sulfuric acid (98%), Nitric Acid (70%), Potassium Permanganate, Hydrogen Peroxide (30%), Hydrochloric acid (30%), Nickel nitrate hexahydrate, Cobalt nitrate hexahydrate, Urea, Na_2S, Melamine, Ethanol were bought from Merck and Sigma-Aldrich. All chemicals were of analytical grade and were utilised as delivered.

Synthesis of porous carbon self-repairing g-C_3N_4

1.5g of Melamine was mixed with 40ml of ethanol and kept in an autoclave at 180°C for 24h. The resultant mixture was filtered and dried. The dried sample was kept in a muffle furnace at 540°C for 4h with a heating rate of 5°C/min to get carbon self-repairing g-C_3N_4 (CCN). 100mg of CCN was mixed with 2ml of HCl (37%) and stirred for 3h. It was then filtered and washed until neutral pH. The filtrate was dispersed in 50ml of 2-Proponol: DI water (1:1) and kept under ultrasonication for 2h. The solution was centrifuged to remove larger particles and dried in an oven at 60°C overnight to get porous carbon self-repairing g-C_3N_4 (pCCN). The bulk g-C_3N_4 (GCN) was produced by thermal treatment of Melamine in a muffle furnace at 540°C for 4h with a heating rate of 5°C/min.

Synthesis of porous carbon self-repairing g-C_3N_4/rGO@$NiCo_2S_4$

GO was synthesized by a procedure earlier reported by us [8]. In the synthesis process, 15mg of GO was mixed with 40ml DI water through sonication. 5mg of pCCN was introduced into the solution and sonicated further for 30min. Further, 6mM $Ni(NO_3)_2 \cdot 6H_2O$, 12mM $Co(NO_3)_2 \cdot 6H_2O$ and 60mM urea was then added while sonication. Then the solution was shifted to a Teflon lined autoclave and placed at 120°C for 10h. The resultant mixture was filtered and washed several times and redispersed into 40ml DI water under sonication. After the addition of 650mg Na_2S, the solution was further sonicated. Then the solution was shifted into a Teflon lined autoclave at 180°C for 8h. The solution was then filtered and washed until neutral pH and dried in an oven at 60°C overnight to get porous carbon self-repairing g-C_3N_4/rGO@$NiCo_2S_4$ (pCRNCS). Carbon self-repairing g-C_3N_4/rGO@$NiCo_2S_4$ (CRNCS) was synthesized by the same procedure except for the addition of CCN instead of pCCN, rGO@$NiCo_2S_4$ (RNCS) by excluding pCCN and $NiCo_2S_4$ (NCS) by excluding both GO and pCCN.

Material Characterization

Powder X-ray diffraction (XRD) were conducted employing Bruker AXS D8FOCUS (Cu-Ka radiation, k = 1.540598 A, 30 kV, 15 mA, scan rate of 1°/min). Raman spectra were obtained using Renishaw basis series with 514 lasers. Scanning Electron Microscopy (SEM) imaging was performed in JEOL JSM 6390LV. Transmission Electron Microscopic (TEM) analysis was performed in TECNAI G2 20 S-TWIN (200 kV) to investigate the morphology.

Results and discussions

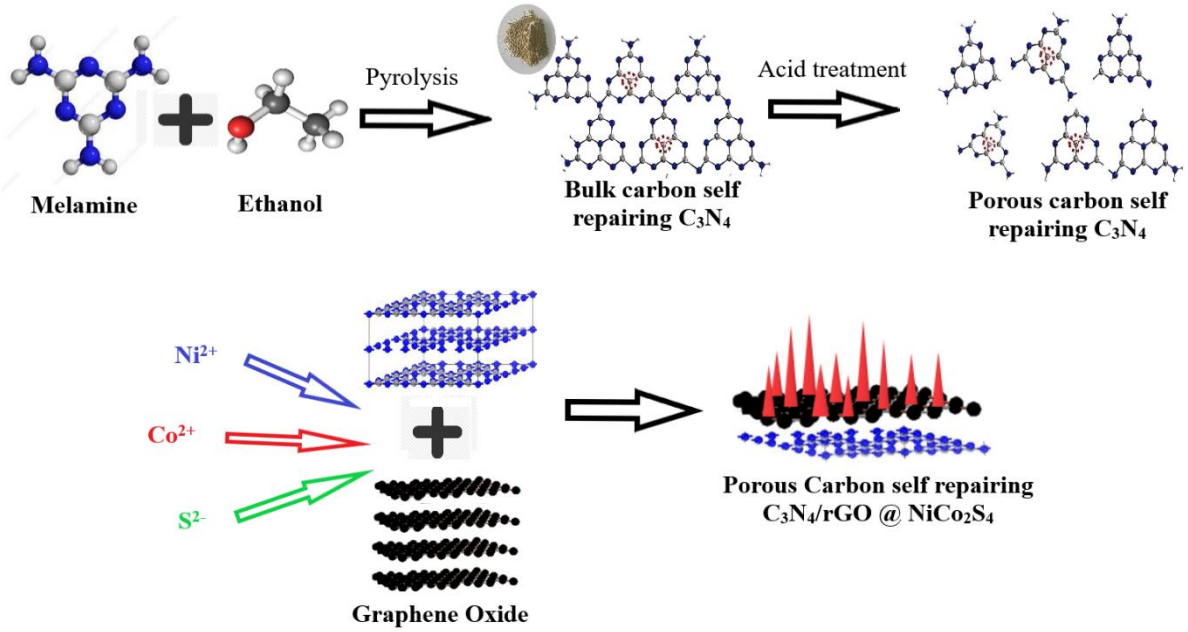

Fig.5.9. Schematic diagram for the synthesis of porous carbon self-repairing g-C_3N_4/rGO@$NiCo_2S_4$ nanocomposite

A novel porous carbon self-repairing g-C_3N_4/rGO@$NiCo_2S_4$ nanocomposite was synthesised by a simple two step hydrothermal procedure (Fig.5.9). Ultrasonication method was initially used to form a homogeneous GO solution. The ionisation of carboxylic, phenolic, and hydroxyl groups on edges and surfaces of GO resulted in the GO sheets being strongly negatively charged when dispersed in water [59]. The initial solvothermal process aided in the introduction of substitutional C atoms in the structure that improved the electronic conductivity of the material due to the extended delocalised π-electrons [48]. As a result of the acid treatment, the larger planes of CCN are broken down into smaller segments, increasing the edge nitrogen and oxygen functional groups [60, 61]. The protonation of CCN lowered the electron cloud density between the interlayer of C and N atoms, which resulted in a decrease

in the interlayer's Van der Waals force, to form few layer CCN [60]. As a result, the ultrasonic exfoliation of the bulk CCN to a few-layer porous CCN was simple. The introduction of porous CCN led to the strong electrostatic interaction with GO and CCN which aided in the suppression of agglomeration of graphene sheets [62]. Further the high nitrogen content and increased active sites in CCN further helped in the nucleation and growth of metal ions [47]. During the addition of Ni^{2+} and Co^{2+} ions, the positively charged metal ions are equally attracted by the GO sheets and porous CCN sheets which effectively reduces the self-agglomeration of $NiCo_2S_4$ and also aids in the self-assembly of all components in the heterostructure [63, 64].

Fig.5.10a shows the FTIR spectrum of the synthesised nanocomposites. The characteristic peak at around 3400 cm^{-1} is attributed to the N-H and -OH groups in the samples. In the FTIR spectra of GCN, CCN and pCCN, the absorption peaks locate at 1242, 1319, 1408, 1568 and 1639 cm^{-1} are attributed to the typical stretching modes of aromatic C−N heterocycles (trigonal$(N-(C)_3)$ (full condensation) and bridging C−NH−C units (partial condensation)) [62]. From the FTIR spectra of RNCS and pCRNCS the peaks position at 564, 628 (symmetrical stretch) and 1092 cm^{-1} (asymmetrical stretch) could be attributed to the Ni–S or Co–S vibrations of $NiCo_2S_4$ [45]. For the pCRNCS sample, all the characteristic peaks of $NiCo_2S_4$ and carbon self-repairing g-C_3N_4 indicating the successful formation of porous carbon self-repairing g-C_3N_4/rGO@$NiCo_2S_4$ nanocomposite.

XRD analysis was done to examine the crystalline phase structure of the synthesised samples. From fig.5.10b, the XRD pattern of g-C_3N_4 (GCN) presented a predominant peak at 27.05° corresponding to (002) stacking of the conjugated aromatic system and a weak peak at 13° indexed to (100) attributes to the in-plane structural packing motif of the tri-s-triazine units [65] (JCPDS Card No. 87-1526). After C-repair, the peak at 13° of bulk g-C_3N_4 widened for CCN due to the interstitial-C atoms bonding with two edge N atoms in the in-plane hollow space [48, 66]. Further, the (002) diffraction peak of carbon self-repairing g-C_3N_4 moved slightly to a greater 2θ value of 27.45°. This should be the result of the crystal lattice distortion following the incorporation of interstitial/substitutional carbon atoms into the g-C_3N_4 structure as demonstrated by earlier investigations [45, 48, 65], confirming the successful creation of carbon self-repairing g-C_3N_4. In addition, this shows a slightly smaller interlayer spacing, which is caused by the 2D g-C_3N_4 sheets being forcedly π-stacked as a result of the extended and complete π-electron system [45]. After the protonation and exfoliation of bulk carbon self-repairing g-C_3N_4 the intensity of (002) peak of pCCN was decreased significantly confirming the formation of few layer CCN [67]. From fig.5.10c, peaks at 2θ values of 16.2º, 26.6º, 31.4º,

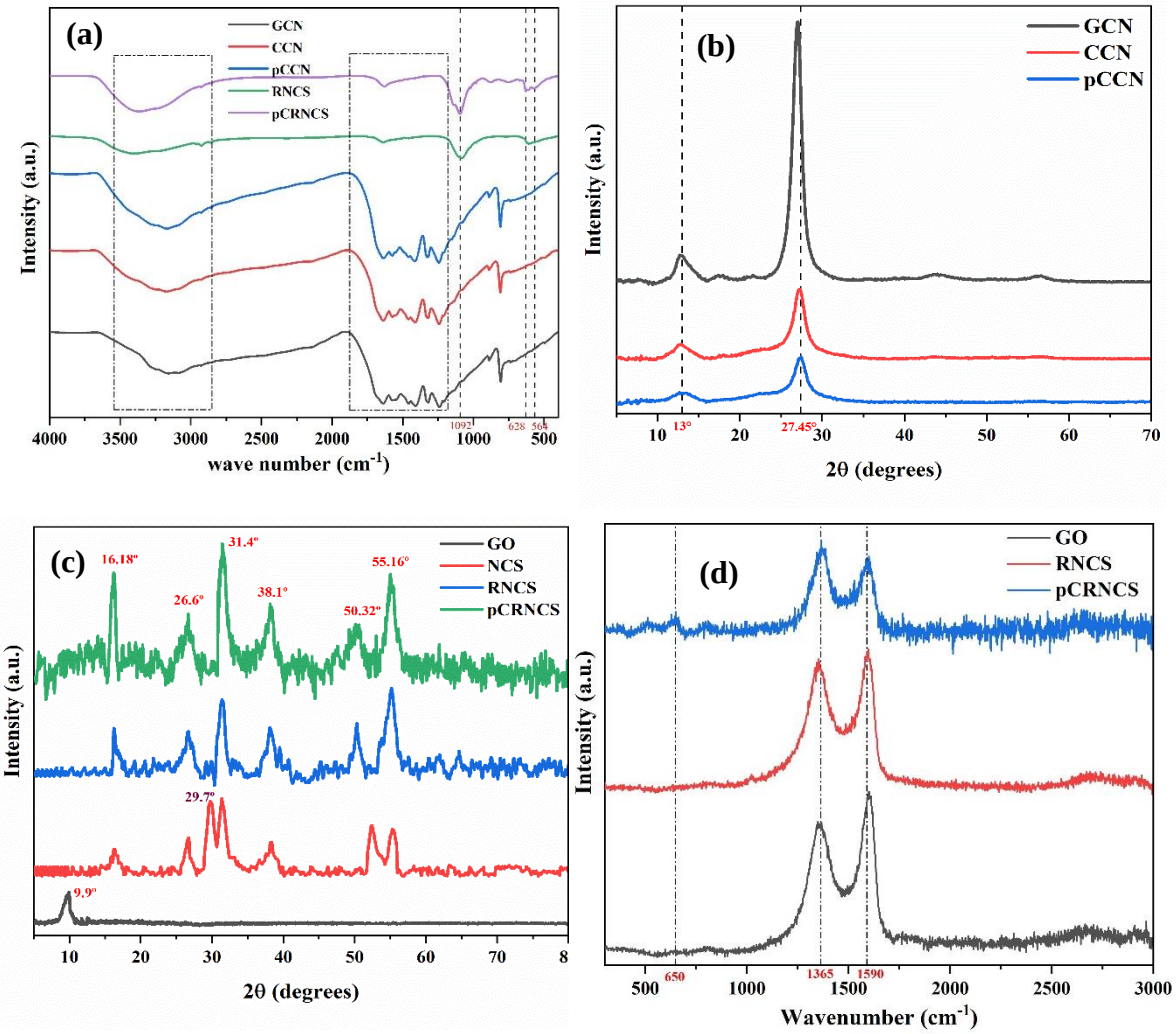

Fig.5.10 (a) FTIR spectra of of GCN, CCN, pCCN, RNCS and pCRNCS (b) XRD spectra of GCN, CCN and pCCN. (c) XRD spectra of GO, NCS, RNCS and pCRNCS. (d) Raman spectra of GO, RNCS, pCRNCS

38.1º, 50.32º and 55.16º corresponds to the (111), (220), (311), (400), (511) and (440) reflections of cubic phase $NiCo_2S_4$ (JCPDS 20-0782) respectively. For pCRNCS sample, all the peaks corresponding to $NiCo_2S_4$ was present and the absence of peak at 9.9º confirms the complete reduction of GO. The broadening of peak corresponding to (002) plane is because of the existence of both pCCN and rGO nanosheets which confirms that the basic structure of both the 2D materials remained unchanged even after the hybridisation process. The additional peaks found at 29.7º of NCS sample is due to the formation of C_9S_8 which was not expected (JCPDS 65-6801). The absence of any additional impurity peaks in pCRNCS sample demonstrates that pure $NiCo_2S_4$ phase was produced. In addition, the weak and broad diffraction peaks of the nanocomposites indicate that low crystallinity was achieved, that is advantageous for the enhancement of electrochemical properties of materials.

Raman spectroscopy was carried out to analyze the disorder and defects in the graphitic structure of the samples. Fig.5.10d displays the Raman spectra of GO, RNCS and pCRNCS samples. The Raman spectra of all the samples shows two characteristics peaks which corresponds to the well-defined D and G bands. The G band, centred at 1590cm^{-1} of pCRNCS

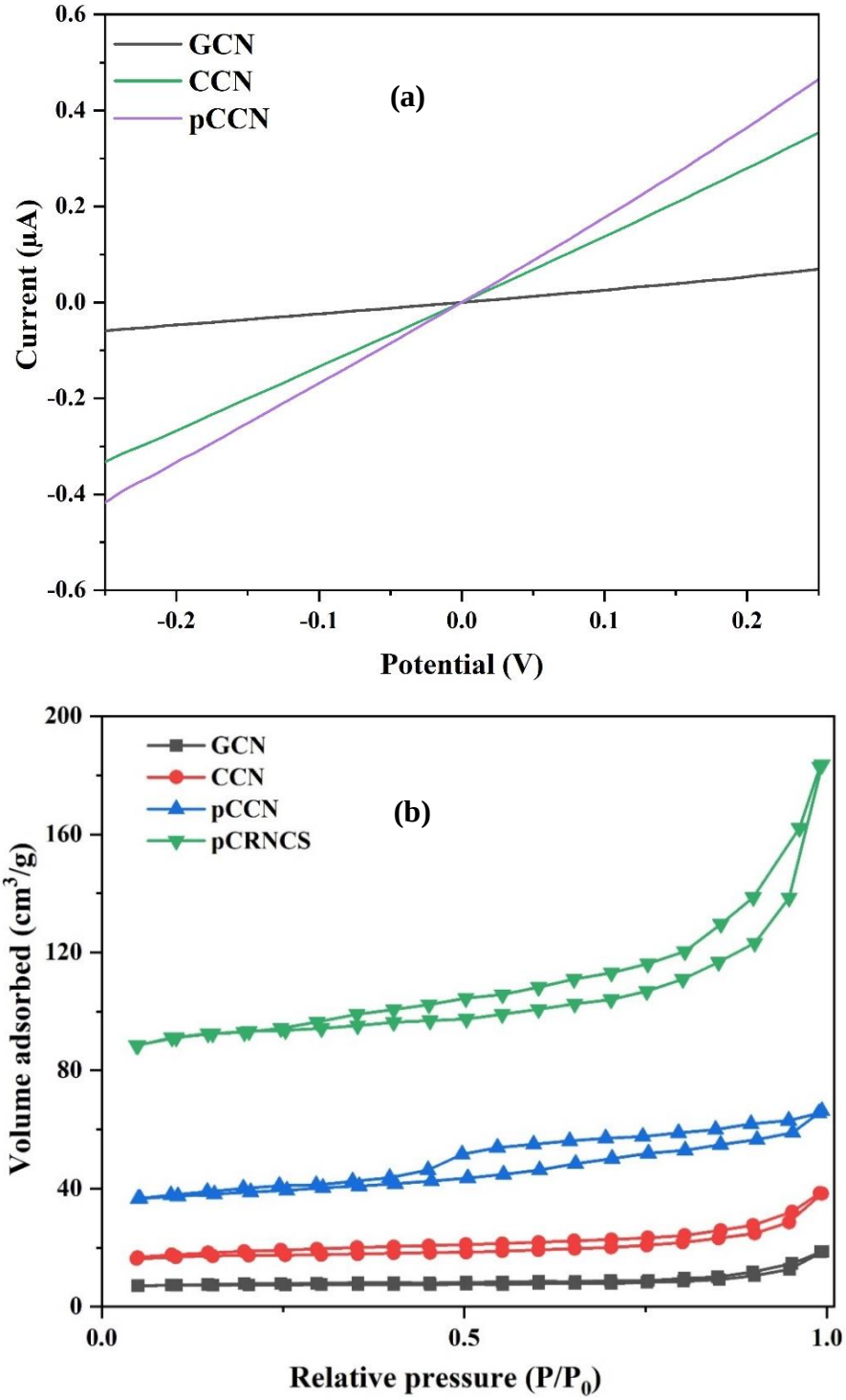

Fig.5.11 (a) I-V plots of GCN, CCN. pCCN (b) N_2 adsorption-desorption isotherm of GCN, CCN, pCCN and pCRNCS

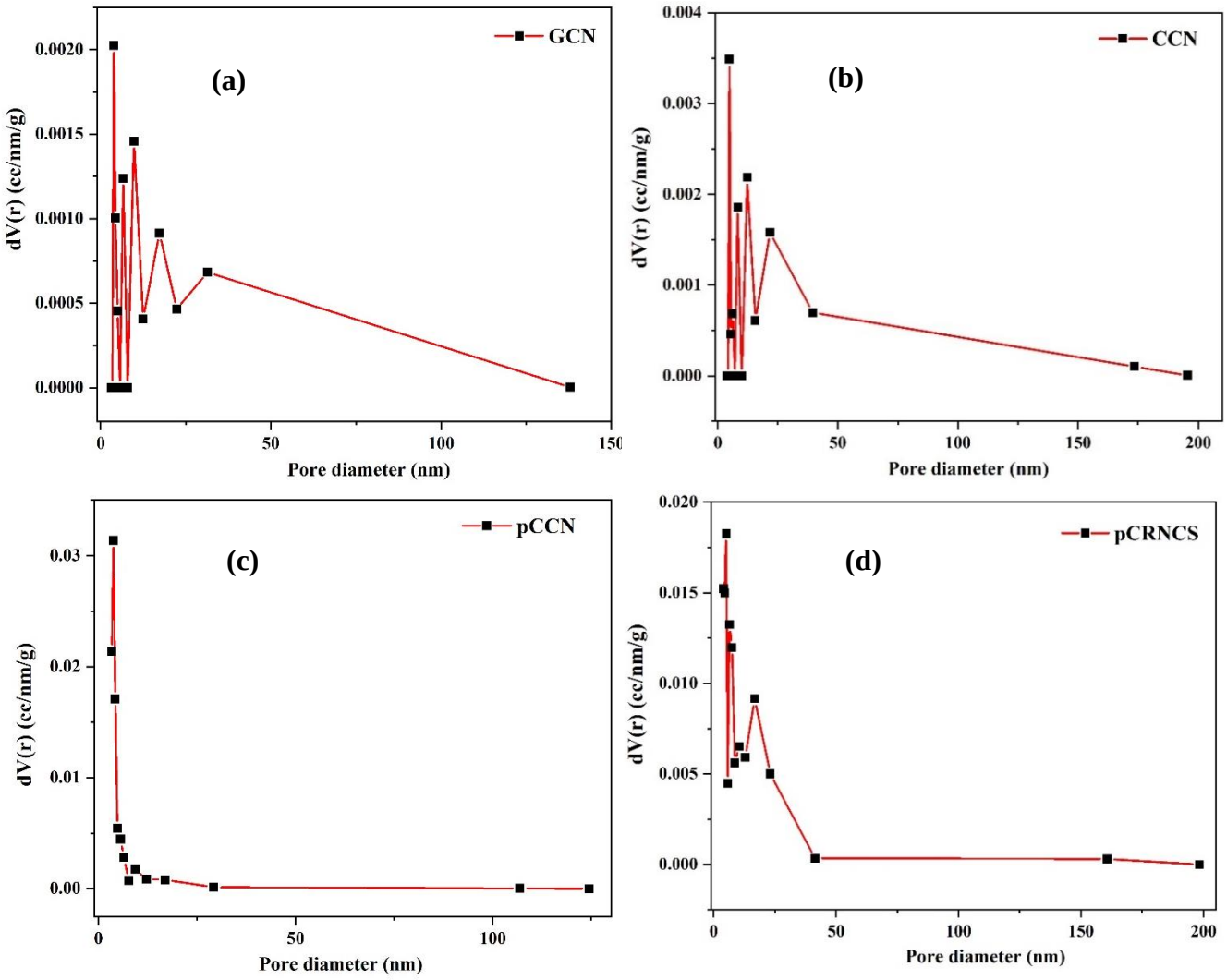

Fig.5.12 Pore size distribution of (a) GCN, (b) CCN, (c) pCCN, (d) pCRNCS

sample, typically results from the E2g phonon of C sp2 atoms, which corresponds to stretching vibrations in the basal plane of graphene. The D band, at approximately 1365cm^{-1}, derives from a breathing k-point phonon with A1g symmetry corresponding to the structural deformity and disorders [19, 68]. The broadened D band is the result of overlapping peaks of C–N vibration at 1285 cm^{-1} [69], the mode of C=N at 1400 cm^{-1}, and the D mode of graphene [70]. Similarly, broadening of G band is the result of overlap between the G bands of g-C_3N_4 and graphene. The shifting closer of D and G bands are attributed to the π-π conjugation of graphene and pCCN layers during restacking process and also the blue shift in G band suggests the formation of few layer heterostructures [71]. The characteristic peak at 680cm^{-1} is associated with the vibration of s-triazine rings (C_3N_3) within the g-C_3N_4 phase [72]. The intensity ratio D to G band (I_D/I_G) implies the structural defects and disorders in the graphitic structures [21]. The

I_D/I_G value increased from 0.84 for GO to 0.94 for RNCS and further elevated to 1.04 for pCRNCS sample, indicating enhanced disorder following the reduction procedure and the existence of more tiny, isolated sp2 graphene domains and g-C_3N_4 domains in pCRNCS sample [22].

As expected, the I–V graphs (Fig.5.11a) confirmed that the slope of pCCN and CCN was greater than that of GCN, indicating that pCCN and CCN has a higher conductivity than GCN according to Ohm's law [48]. This confirms the creation of extended delocalized π-electron by the substitutional or interstitial C atoms in the structure which contributed to the enhanced electrical conductivity of CCN and pCCN samples.

The BET analysis was performed to study the surface area and pore size distribution for GCN, CCN, pCCN and pCRNCS samples. The N_2 adsorption-desorption isotherm (Fig.5.11b) of all the samples shows a typical type IV isotherm characteristic with H3 hysteresis loop, indicating the existence of mesoporous structure [73]. Using the Brunauer−Emmett−Teller (BET) method, the specific surface area (SSA) of GCN, CCN, pCCN and pCRNCS are found to be 23.4, 64.08, 132.19 and 268.08 m^2/g respectively. The high SSA of pCCN confirms the formation of few layers CCN after the acid treatment which is in agreement with the XRD results. The high surface area of pCRNCS is due to the successful formation of pCCN/rGO heterostructure in which porous pCCN is stacked alternatively in between graphene nanosheets. The formation of heterostructure reduces the agglomeration of individual constituents thereby giving high surface area. From the pore size distribution graph (Fig.5.12), the mesoporous nature of the samples is confirmed with the presence of mesopores at around 3.41-29.25 nm for all samples. Few macropores can also be observed. The pCCN sample showed high pore volume of 0.45 cc/g in comparison with CCN (0.21 cc/g) and GCN (0.12 cc/g) which shows the porous nature of pCCN. The pCRNCS sample showed high pore volume of 0.76 cc/g. The porous structure with high pore volume of pCRNCS provide more active sites for electrochemical reactions and boosts the supercapacitor performance of the material [74].

The TEM images were acquired to analyse the morphology of pCRNCS sample in Fig.5.13. The morphology reveals atomic thin rGO nanosheets with good transparency and clear wrinkles and folds. The transparent rGO sheets obtained suggests that rGO formed are mostly of single or few layers of graphene. The porous CCN nanosheets and rGO layers are also observed with clear lattice fringes with an interplanar distance of 0.33nm and 0.36nm respectively (Fig.5.13c), which is consistent with previously reported literatures [21, 61]. The

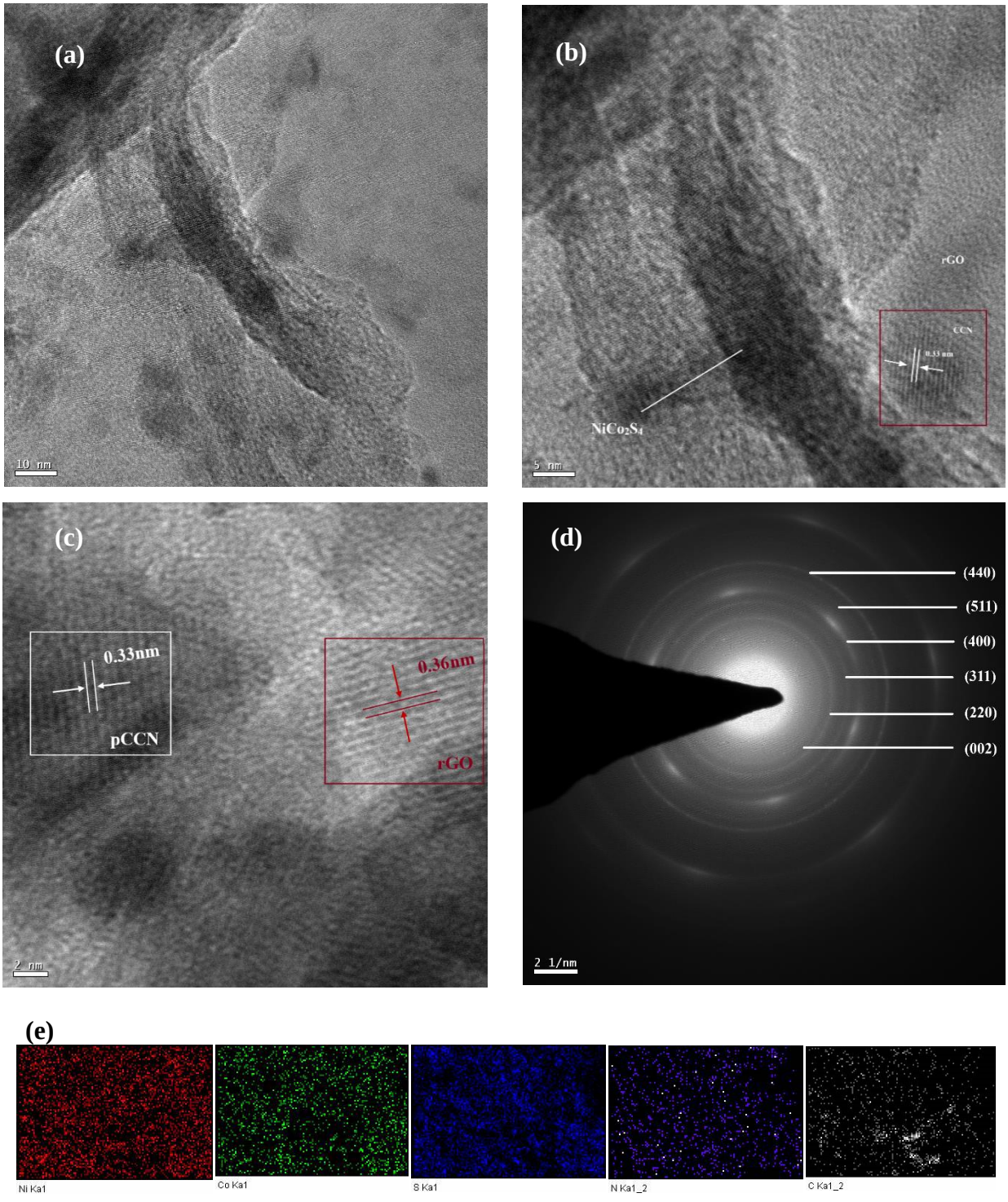

Fig.5.13 (a-b) TEM and (c) HRTEM images of pCRNCS sample (d) SAED pattern of pCRNCS sample (e) EDS mapping of pCRNCS sample

multiple overlapped layers of pCCN and rGO suggests that porous CCN nanosheets are well embedded into the rGO layers. Pure CCN after acid pre-treatment, produced exfoliated pCCN exhibiting thin layer structure and no discernible CCN bulk domains. The well dispersed pCCN in water further incorporated the 2D structures of pCCN with GO forming a more compact

2D/2D sheet-on-sheet structure. The $NiCo_2S_4$ grown over 2D/2D pCCN/rGO heterostructure are also seen (Fig.5.13b). Furthermore, the TEM images clearly show the tight contact and interface between $NiCo_2S_4$, rGO, and g-C_3N_4 forming a coherent and distinguished heterojunction nanostructure [75]. The broad contact interface and high electron mobility of rGO make possible a strong charge flow and a rapid charge transfer. The SAED pattern (Fig.5.13d) confirms the polycrystalline nature of the sample, and the diffraction rings can be indexed to (220), (311), (400), (511) and (440) planes of cubic phase $NiCo_2S_4$ which is in agreement with XRD results. The weak and diffuse ring corresponds to (002) plane of pCCN and rGO seen in the SAED pattern is consistent with several investigations [61, 76-78]. The EDS mapping shown in Fig.5.13e indicates a uniform distribution of Ni, Co, S, N and C, confirming the successful formation of carbon self-repairing g-C_3N_4/rGO@$NiCo_2S_4$ nanocomposite.

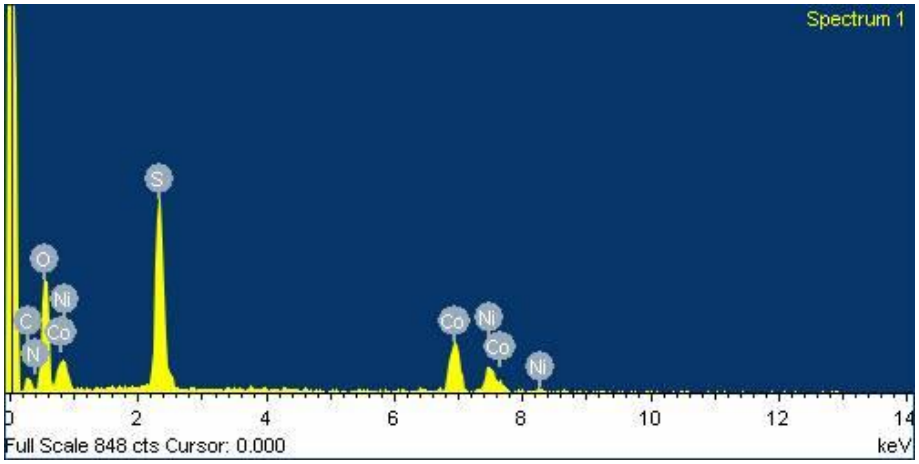

Element	Weight%	Atomic%
C K	14.31	24.08
N K	6.43	9.27
O K	38.26	48.33
S K	14.74	9.29
Co K	17.30	5.93
Ni K	8.96	3.09
Totals	100.00	

Fig. 5.14. EDS spectrum and elemental composition of pCRNCS sample

EDS spectrum and elemental composition of pCRNCS sample is shown in Fig.5.14. The EDS spectrum of pCRNCS shows almost double the nitrogen content than that of RNCS (Fig.5.4). Also, it showed the highest oxygen content in comparison to other samples. This is attributed to the high nitrogen and oxygen content due to the introduction of pCCN into the nanocomposite.

Electrochemical performance analysis

The electrochemical performance analysis of all the samples in alkaline electrolyte media. Fig.5.15a describes the cyclic-voltammogram of all samples at a scan rate of 20mV/s. The shape of CV of all samples remained the same even after the addition of rGO and pCCN. The rGO aided in the improvement of electrochemical surface area and pCCN enhanced the active

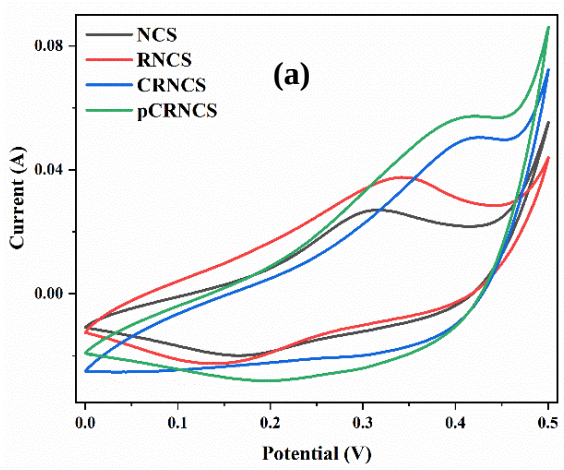
NCS
RNCS
CRNCS
pCRNCS
(a)
Current (A)
Potential (V)

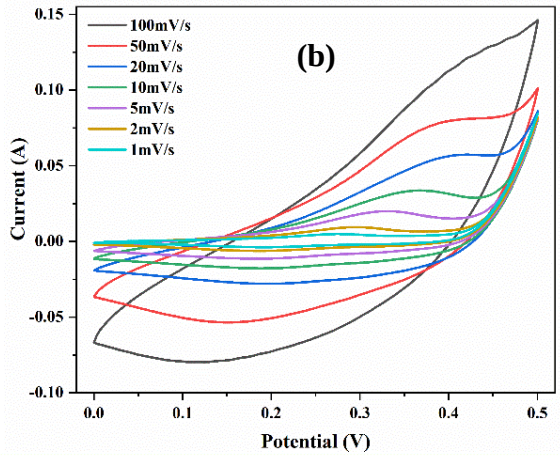
100mV/s
50mV/s
20mV/s
10mV/s
5mV/s
2mV/s
1mV/s
(b)
Current (A)
Potential (V)

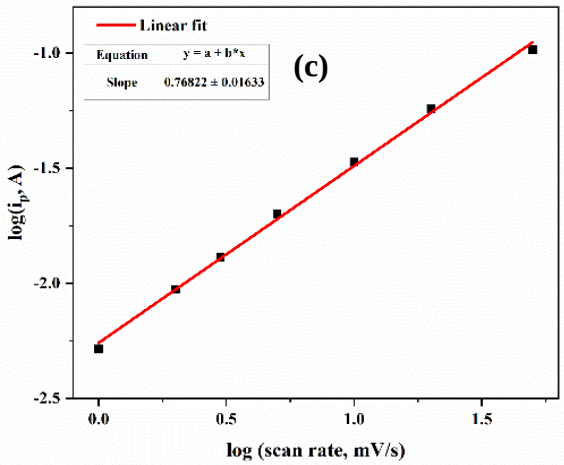
Linear fit
Equation y = a + b*x
Slope 0.76822 ± 0.01633
(c)
log(i_p, A)
log (scan rate, mV/s)

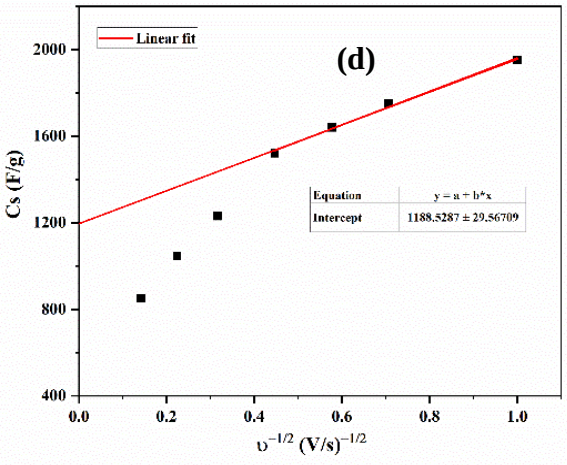
Linear fit
(d)
Cs (F/g)
Equation y = a + b*x
Intercept 1188.5287 ± 29.56709
υ^-1/2 (V/s)^-1/2

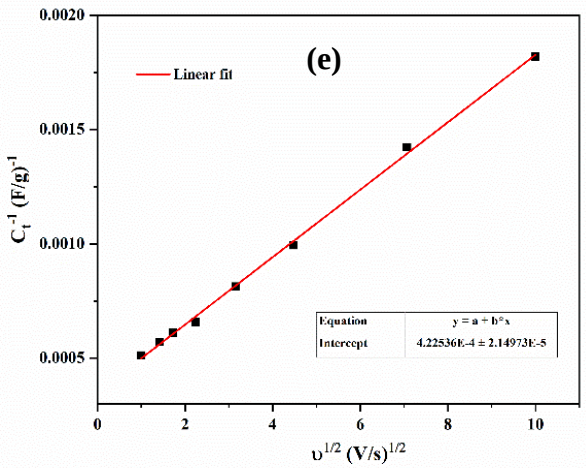
Linear fit
(e)
C_t^-1 (F/g)^-1
Equation y = a + b*x
Intercept 4.22536E-4 ± 2.14973E-5
υ^1/2 (V/s)^1/2

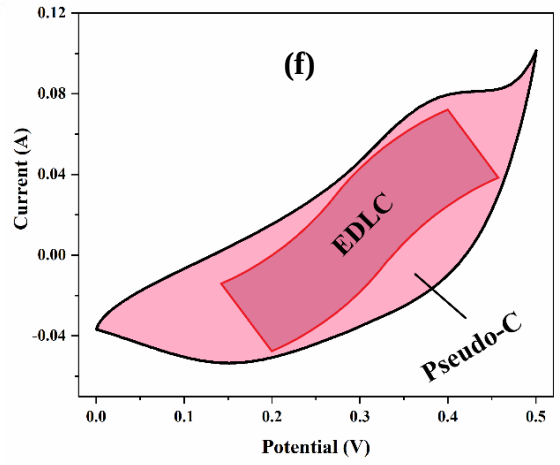
(f)
EDLC
Pseudo-C
Current (A)
Potential (V)

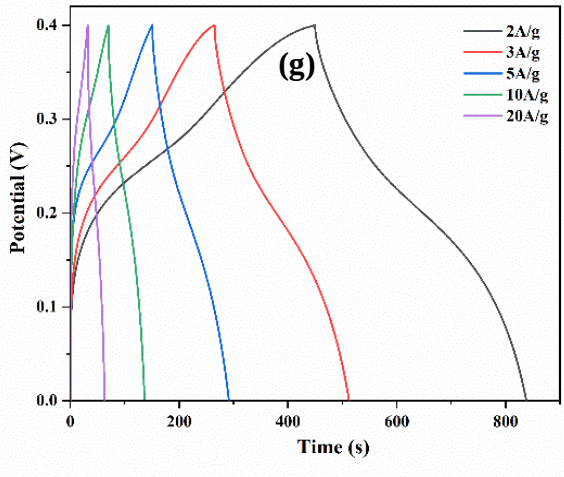
2A/g
3A/g
5A/g
10A/g
20A/g
(g)
Potential (V)
Time (s)

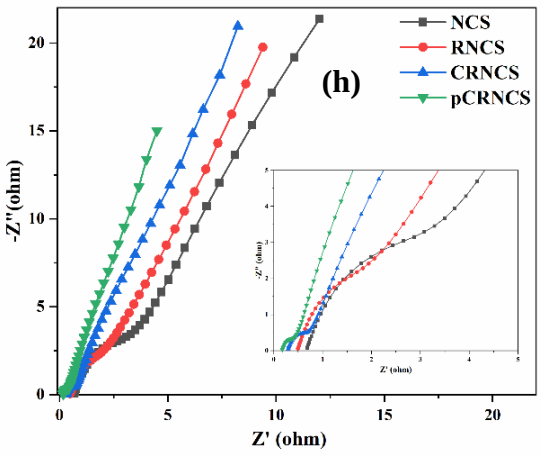
NCS
RNCS
CRNCS
pCRNCS
(h)
-Z''(ohm)
Z' (ohm)

Fig.5.15 (a) CV curves of NCS, RNCS, CRNCS and pCRNCS at 20mV/s. (b) CV curves of pCRNCS at different scan rates. (c) Relationship between log(peak current) and log(scan rate). (d) Relationship between Specific capacitance and $(\text{scan rate})^{-1}$. (e) Relationship between $(\text{Specific capacitance})^{-1}$ and scan rate. (f) CV of pCRNCS at 50mV/s (g) GCD curves of pCRNCS at different current densities. (h) EIS curves of NCS, RNCS, CRNCS and pCRNCS.

edge nitrogen and oxygen functional groups. The charge storage mechanism of rGO and pCCN are predominantly EDLC and hence the shape of CV of the samples remains the same even after the addition of rGO and pCCN. The redox peaks are clearly visible in the CV of all samples due to the Faradaic redox activity effectively occurred in the electrode by Ni^{2+}/Ni^{3+}, Co^{2+}/Co^{3+}, and Co^{3+}/Co^{4+} ionic conversion processes.

The corresponding redox processes are represented as [79]:

$NiCo_2S_4 + 2OH^- + H_2O \longleftrightarrow NiSOH + CoSOH + 2e^-$ ..... (1)

$NiSOH + OH^- \longleftrightarrow NiSO + H_2O + e^-$..... (2)

$CoSOH + OH^- \longleftrightarrow CoSO + H_2O + e^-$ ..... (3)

The magnitude of area bounded by the CV curve is in the order NCS<RNCS<CRNCS <pCRNCS. The pCRNCS electrode showed highest CV area and current density in comparison with other samples. This is due to the improved electrochemical performance by the combined effect of high surface area rGO and extended highly reactive region and defects in pCCN which facilitated the nucleation and confined growth of $NiCo_2S_4$ in the framework. Also, the improved electronic conductivity and activity of CCN than GCN due to the formation of extended delocalized π-electron by the substitutional or interstitial C atoms in the structure enhanced the specific capacitance [48]. On the other hand, surface charge modification of CCN by acid treatment helped in the formation of a well-defined rGO/pCCN heterostructure by π-π interaction with large surface area and porosity [61]. Further, the optimum use of both EDLC and pseudocapacitive materials prevented the agglomeration of particles as pCCN layers embedded well in between graphene nanosheets and the confined growth of $NiCo_2S_4$ in between layers to form very few layered nanocomposite while restacking process [21].

Fig.5.15b shows the CV of pCRNCS at various scan rates from 1mV/s to 100mV/s. All the CV curve retained their shapes while the position of redox peaks shift slightly as the scan rate is increased. This suggests the enlarged electrode polarisation and fast reaction kinetics of the electrode material [80, 81]. Concentration polarisation, charge transfer polarisation, and other polarisation effects predominate at faster scan rates, increasing the overpotential and

preventing the faradaic processes from occurring, resulting in an increase in peak separation. For further analysis, the scan rate and current density of the material was plotted, as in Fig.5.15c. In general, the peak current (i_p) in CV curves follows a power-law as the scan rate changes, as given by the equation:

$$i_p = a\vartheta^b \ldots\ldots\ldots\ldots\ldots\ldots (4)$$

$$\log(i_p)=\log(a)+b\log(\vartheta) \ldots\ldots\ldots (5)$$

where, the co-efficients 'a' and 'b' are constants, i_p=peak current (A) and ϑ=scan rate (mV/s). From eq.(5), 'b' is slope of $\log(i_p)$ vs. $\log(\vartheta)$ plot. The energy storage mechanism is surface controlled (EDLC process) when b=1, diffusion controlled (pseudocapacitive process) when b=0.5 and combined effect of EDLC and pseudocapacitive when 0.5<b<1. Thus, for a supercapacitor the ideal value of b should be ~1 and for battery material b should be ~0.5. So, the electrode material can be distinguished using the charge storage mechanism. Fig.5.15c shows the linear plot of $\log(i_p)$ vs. $\log(\vartheta)$ with a slope, b=0.768 which implies that the energy storage process in pCRNCS is determined by the combined effect of both EDLC and pseudocapacitive processes. The drop in b value between pCRNCS and RNCS (Fig.5.7c) is attributable to the higher pseudocapacitive contribution by the participation of edge nitrogen atoms of pCCN nanosheets which proves the successful integration of pCCN into the heterostructure.

Trasatti method was employed to further differentiate the capacitance contribution by charge storage mechanism in the material. The specific capacitance was computed using the eq [33, 34]:

$$C_s = \frac{A}{2*\vartheta*V} \ldots\ldots\ldots\ldots\ldots (6)$$

The C^{-1} vs $\vartheta^{\frac{1}{2}}$ plot will reveal a linear connection with the assumption of semi-infinite diffusion of ions (i.e., freely diffuse to the electrode/electrolyte interface from bulk electrolyte), and the intercept of the fitted line will reveal the reciprocal of total capacitance (C_t). Due to the electrode's inherent resistance and departure from semi-infinite ion diffusion (Fig.5.15e), the data points acquired at larger scan rates departed from the linear relationship and the corresponding data points were ignored during the linear fitting process. The relationship can be described as in eq [34]:

$$C_s{}^{-1} = constant * \vartheta^{\frac{1}{2}} + C_t{}^{-1} \ldots. (7)$$

where, $C_t = C_{pseudo} + C_{EDL} \ldots\ldots (8)$

The plot between gravimetric capacitance (C_s) and $\vartheta^{-\frac{1}{2}}$ will also show a linear connection with the same assumption of semi-infinite ion diffusion, and the y-intercept of the fitted line will show EDL capacitance (C_{EDL}). So, from eq.(8),

$$C_{pseudo} = C_t - C_{EDL} \text{ ……...(9)}$$

The capacitance contribution can be found out by following eq:

$$C_{EDL}\% = \frac{C_{EDL}}{C_t} * 100\% \text{ ……... (10)}$$

$$C_{pseudo}\% = \frac{C_{pseudo}}{C_t} * 100\% \text{.....(11)}$$

From fig.5.15d, C_{EDL}=1188F/g is the contribution of EDL capacitance and from fig.5.15e, the inverse of y-intercept gives the total capacitance, C_t=2366 F/g. From eq.(9), $C_{pseudo} = 1178\text{F/g}$. From eq.(10) and (11), $C_{EDL}\% = 50.21\%$ and $C_{pseudo}\% = 49.79\%$ [Fig.5.15f]. This suggests that the energy storage process in pCRNCS sample is caused by the combined effect of both surface controlled and diffusion controlled processes. After Trasatti analysis, the higher pseudocapacitive contribution in pCRNCS sample than that in the case of RNCS is in agreement with the power plot analysis. The reason could be the higher Nitrogen content in the pCCN that takes part in the electrochemical reactions. The hierarchical porous rGO/pCCN heterostructure with uniformly grown redox $NiCo_2S_4$ gives rise to improved specific capacity and exceptional rate performances by increasing the electrochemical active sites available for the adsorption of electrolyte ions and quick Faradaic pseudocapacitance processes [82].

Fig.5.15g displays the GCD curve of pCRNCS at various current densities. The fact that all of the GCD plots are non-linear and that the associated voltage plateaus are almost identical to those on the CV curve, which is evidence of the pseudocapacitive nature of the nanocomposite. To compute the specific capacitances using GCD curves, the following equation was used:

$$\text{Specific Capacitance, } C_s = \frac{I.\Delta t}{m.\Delta V} \text{ F/g ……..(11)}$$

where, I = discharge current (A), Δt = discharge time (s), m = mass of the electroactive material (g), and V = potential window (V). According to the GCD curve, pCRNCS sample presented an outstanding specific capacitance of 1938F/g at a current density of 2A/g, that is remarkably high in comparison to electrodes based on metal oxides or metal sulphides which have been reported earlier [Table.5.2]. The specific capacitances calculated are 1850F/g, 1742F/g, 1655F/g and 1548F/g at current densities 3A/g, 5A/g, 10A/g and 20A/g. Even though specific capacitance reduces with increase in current density, the material displayed a specific capacitance of 1548F/g at 20A/g indicating exceptional rate capability.

The reaction kinetics of the electrodes were studied by performing Electrochemical Impedance Spectroscopy (EIS). The Nyquist plot [Fig.5.15h] of all the samples have the same shape, which is a semicircle with a sloped line. The x-intercept in the beginning of the semicircle defines the Equivalent series resistance (R_s) of the nanocomposite and the diameter of semi-circle shows the charge transfer resistance (R_{ct}). The ESR comprises the contact resistance at the boundary of electrolyte and electrode, the intrinsic resistances of the electrode active material, and the bulk resistance of the electrolyte [83]. The slope in the low frequency zone of the plot defines Warburg resistance that occurs as a result of the diffusion of ions from electrolyte into the electrode. When compared to other materials, the pCRNCS material displayed the steepest slope, which indicates that ions move through it more quickly with less diffusion resistance. Similarly, R_s and R_{ct} of pCRNCS material was much smaller than other materials suggesting lower charge transfer resistance and bulk resistance. This is because pCCN-NSs have a high nitrogen content on their surface, which makes it easier for electrolyte ions to be adsorbed and increases the hydrophilicity of composite material, resulting in improved wettability and rapid movement of electrolyte ions within the electrode material. The greater water solubility of pCCN prevents polymeric material from aggregating on graphene oxide layers, as more channels are accessible for ion transport inside the pCRNCS sample. As a result, huge polymeric chunks that previously restricted ion movement in CRNCS sample are removed due to acid treatment.

The enhanced electrochemical properties of pCRNCS material are because of the unique interlinked hierarchical structure of the composite in which porous CCN was well embedded into rGO nanosheets and the uniform growth of $NiCo_2S_4$ over the heterostructure. The substitutional-carbon crosslinking led to the formation of extending delocalized π-electrons via activation of inert g-C_3N_4 and acid treatment of CCN resulted in improved electron conductivity of pCRNCS material by fracturing the polymeric structures and inducing higher contents of edge N and O doping of the nanocomposite. The intense crosslinking among rGO and porous C-C_3N_4, resulting from the extended π-conjugated planar layers of C-C_3N_4 and a greater surface area aided in the formation a highly porous heterostructure. The confined growth of $NiCo_2S_4$ over rGO/pCCN heterostructure provides better diffusion pathways for electrolyte ions and ion-buffering reservoirs while charge and discharge as well as multiple oxidation states for the Faradaic redox processes.

An asymmetric supercapacitor (ASC) was developed to study the practical applications of the synthesised pCRNCS sample. The ASC was fabricated using pCRNCS as the anode electrode and activated carbon (AC) as the cathode material in a 3M KOH electrolyte. The mass loading

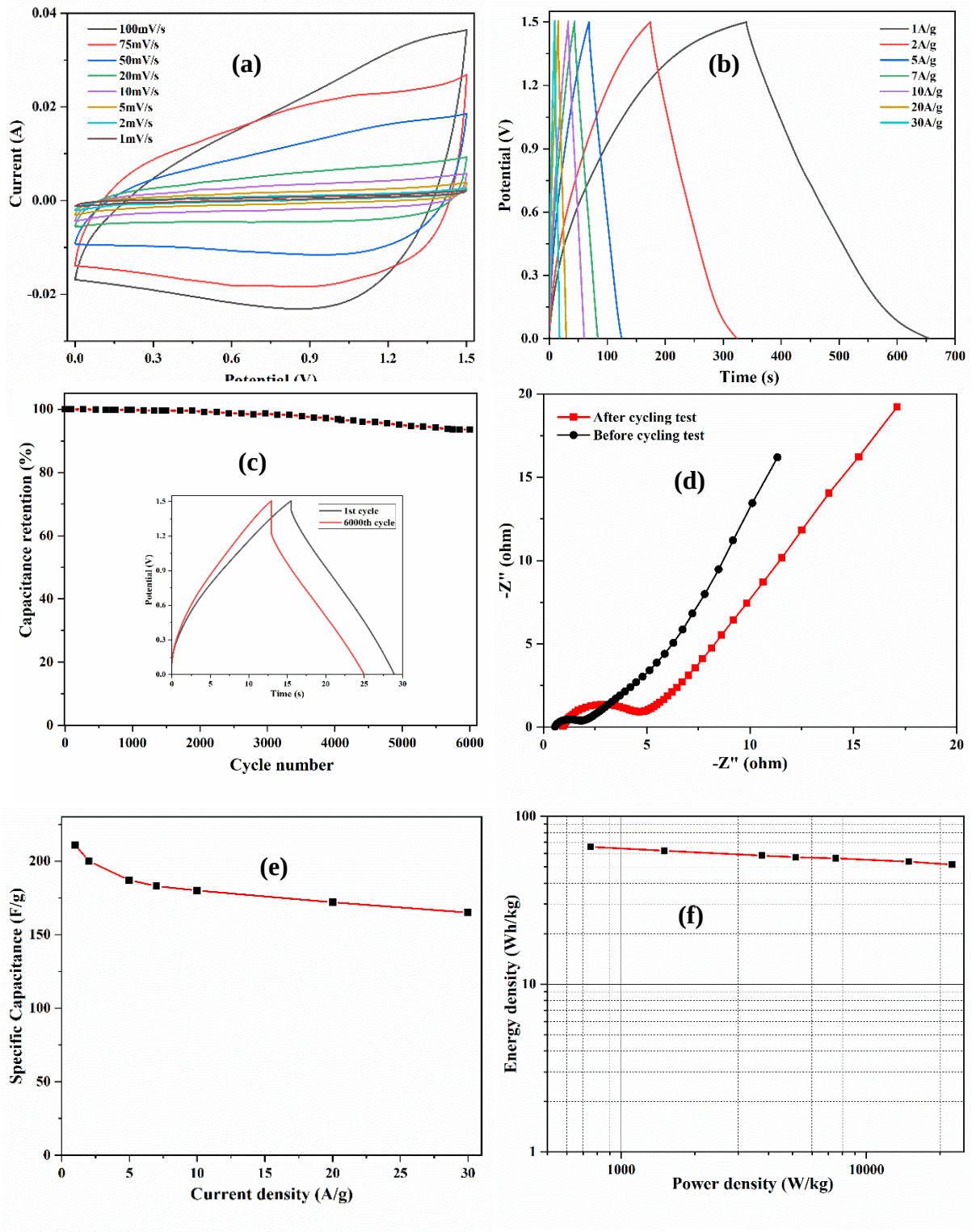

Fig.5.16 (a) CV of pCRNCS//AC at different scan rates (b) GCD of pCRNCS//AC at different current densities (c) Capacitance retention of pCRNCS//AC after 6000 cycles at 20A/g. inset: initial and final GCD curve after 6000 cycles (d) EIS spectra of pCRNCS//AC before and after cycling stability test (e) Specific capacitance of pCRNCS//AC at different current densities (f) Power density Vs. Energy density plot of pCRNCS//AC

of the electrodes was done according to the mass balancing equation (Eq. (1)). Fig.5.16a presents the CV of as fabricated pCRNCS//AC ASC at different scan rates from 1 to 100mV/s. All the CV curves retained the same shape even at 100mV/s suggesting the exceptional electrochemical stability of the device. The representative GCD curves [Fig.5.16b] of the ASC at various current densities from 1 to 30A/g. The specific capacitance was computed according to eq(11). The pCRNCS//AC ASC showed excellent specific capacitance of 211F/g at 1A/g. Also, the specific capacitance was calculated to be 200F/g, 187F/, 183F/g, 180F/g, 172F/g and 165F/g at current densities of 2A/g, 5A/g, 7A/g, 10A/g, 20A/g and 30A/g respectively. The lower capacitance value at higher current densities primarily corresponds to the Ohmic drop (ESR), which makes a significant contribution, and the sluggish electrochemical reaction kinetics at such higher current densities. Most of the as-prepared materials cannot effectively engage in electrochemical activities at greater current densities, contributing to poor capacitance values. The cycling stability of pCRNCS//AC ASC was analysed for 6000 cycles at 20A/g. The device exhibited an outstanding cycling stability of 93.6% after 6000 cycles [Fig.5.16c]. The inset shows 1st and 6000th GCD cycle of the cycling stability test. Fast redox reactions result in composition destruction due to irreversible chemical reactions, and the intercalation/deintercalation of electrolyte ions during charge-discharge cycles to balance the total charge will also inflict mechanical stress on the physical structure of the electrode material. Hence, repeated charge-discharge cycles will undoubtedly result in mechanical and electrical defects that lower initial performance attributed to the reduction of active material mass. The better cycling stability of the device is because of the shielding effect by rGO/pCCN heterostructure on $NiCo_2S_4$ from shrinking and swelling during fast charge/discharge process. EIS analysis [Fig.5.16d] was done to investigate the charge storage kinetics of the device before and after the cycling test. The R_s value before and after stability test were found after fitting to be 0.6Ω and 1.27Ω respectively. Similarly, R_{ct} before and after stability test was 0.96Ω and 3.8Ω respectively. The substantial increase in Rs and Rct readings following the stability test is attributable to the degradation that results from repeated use for the reasons previously described. The delamination of electrode materials from the substrate also contribute to the diminishing of the specific capacitance [84]. The device showed excellent retention [Fig.5.16e] of 78.2% even at a high current density of 30A/g.

The energy density and power density are calculated using the eqs:

$$\text{Energy density, } E_s = \frac{C_s(V)^2}{2} * \frac{1}{3.6} \text{ Wh/kg}$$

$$\text{Power density, } P_s = \frac{E_s}{\Delta t} * 3600 \text{ W/kg}$$

where, Cs is the specific capacitance and V is the potential window. Fig.5.16f shows the Ragone plot derived from the GCD curves. The ASC device presented an exceptional energy density of 66Wh/kg at a power density of 751W/kg. It was discovered that the energy density of the ASC used in this work were superior to those of several comparable ASCs [30, 85-90]. The high energy density is attributed to the large cell voltage and high specific capacitance of the device.

Sample	**Specific Capacitance of electrode (F/g)**	**Power Density (W/kg)**	**Energy Density (Wh/kg)**
3D CuS /rGO [85]	37.2 (10A/g)	681	16.7
CMT/$NiCo_2S_4$ [86]	1210 (05A/g)	753	28.1
carbon-coated spherical $NiCo_2S_4$ [87]	949 (1A/g)	799	43.8
Mesoporous $NiCo_2S_4$ [30]	1440 (3A/g)	245	28.3
rGO/$NiCo_2S_4$ [89]	1059 (2A/g)	400	38.8
$NiCo_2S_4$ NSs/P-g-C_3N_4 [88]	506 (1A/g)	200	16.7
honeycomb-like $NiCo_2S_4$/rGO [90]	1186 (1A/g)	400	46.4
porous carbon self-repairing g-C_3N_4/rGO/$NiCo_2S_4$ [Present work]	**1938 (2A/g)**	**751**	**66**

Table.5.2. Electrochemical performance comparison of various previously reported metal sulphide based composite materials

5.4 Conclusion

In summary, a novel hierarchical porous N, S doped $NiCo_2S_4$/rGO hybrid nanocomposite was synthesized by in-situ growth of $NiCo_2S_4$ into porous rGO framework by a simple hydrothermal route. The optimum amount of materials were identified by synthesising samples at different ratios and evaluating its electrochemical performances. The optimum use of materials showed improved nucleation and confine growth of $NiCo_2S_4$ into the rGO nanosheets. Also, the wedging-in of $NiCo_2S_4$ nanoneedles into the graphene layers prevented the aggregation of graphene layers while restacking, providing better conductivity and high surface area due to formation of very few layer graphene nanosheets. The N,S dual doping further enhanced the electrochemical activity by introducing defects in the crystal structure by replacing the lattice C atoms thereby rendering the graphene structure more disordered. The GNCS3 sample showed exceptional electrochemical properties with a specific capacitance of 1640F/g at 1A/g current density. These results evidently suggests the potential use of GNCS3 as an excellent supercapacitor material. The all-solid-state GNCS3//AC ASC fabricated showed outstanding electrochemical activity with a specific capacitance of 135F/g at 1A/g, excellent capacitance retention of 92.5% after 5000 cycles and highest energy density of 27Wh/kg at an power density of 600W/kg.

A facile hydrothermal procedure was proposed for the confined growth of $NiCo_2S_4$ on porous carbon self-repairing g-C_3N_4/rGO heterostructure as hybrid material for supercapacitor electrodes. The formation of 2D/2D porous carbon self-repairing g- C_3N_4/rGO heterostructure acted as a framework and backbone for the electron conduction and confined growth of $NiCo_2S_4$ within the framework. The as-synthesised pCRNCS electrode presented exceptional specific capacitance (1938F/g at current density of 2A/g). The excellent electrochemical activity is due to the 2D/2D heterostructure assembly of high surface area rGO and extended highly reactive region and defects in pCCN which facilitated the nucleation and confined growth of $NiCo_2S_4$ in the framework. The constructed pCRNCS//AC ASC exhibited remarkable electrochemical properties, including a specific capacitance of 211F/g at 1A/g, an exceptional capacitance retention of 93.6% after 6000 cycles, and the maximum energy density of 66Wh/kg at a power density of 751W/kg. The exceptional capacitive behaviour of porous carbon self-repairing g-C_3N_4/rGO@$NiCo_2S_4$ makes it the best choice as electrode material for supercapacitors.

Bibliography

[1] Deka, B. K., Hazarika, A., Lee, S., Park, Y.-B. and Park, H. W. Triboelectric-nanogenerator-integrated structural supercapacitor based on highly active P-doped branched Cu–Mn selenide nanowires for efficient energy harvesting and storage. *Nano Energy*, 73:104754, 2020.

[2] Sarmah, S., Kakati, B. K. and Deka, D. Recent advancement in rechargeable battery technologies. *Wiley Interdisciplinary Reviews: Energy and Environment*:e461, 2022.

[3] Sarmah, S., Gohain, M. and Deka, D. Study of the Effect of Biomass-Derived N-Self Doped Porous Carbon in Microbial Fuel Cell. In *Proceedings of the 7th International Conference on Advances in Energy Research*, pages 1155-1163, 2021. Springer.

[4] Bora, C., Sharma, J. and Dolui, S. Polypyrrole/sulfonated graphene composite as electrode material for supercapacitor. *The Journal of Physical Chemistry C*, 118(51):29688-29694, 2014.

[5] Ms, N. A. D., Ms, S. N., Mr, S. S., Ms, R. B., Ms, S. R., Mr, W. I. S. and Swain, B. P. Investigation of chemical bonding and supercapacitivity properties of Fe3O4-rGO nanocomposites for supercapacitor applications. *Diamond and Related Materials*, 104:107756, 2020.

[6] Sarkar, C., Nath, J., Bhuyan, S. and Dolui, S. K. Multifunctional ternary nanocomposites of Ni/Polypyrrole/Reduced graphene oxide as supercapacitor and electrocatalyst in methanol oxidation. *ChemistrySelect*, 4(9):2529-2537, 2019.

[7] Devi, M. and Kumar, A. Surface modification of reduced graphene oxide-polyaniline nanotubes nanocomposites for improved supercapacitor electrodes. *Polymer Composites*, 41(2):653-667, 2020.

[8] Panicker, N. J., Das, J. and Sahu, P. Synthesis of highly oxidized graphene (HOG) by using HNO3 and KMnO4 as oxidizing agents. *Materials Today: Proceedings*, 46:6270-6274, 2021.

[9] Yang, J., Yu, C., Fan, X., Zhao, C. and Qiu, J. Ultrafast self-assembly of graphene oxide-induced monolithic NiCo–carbonate hydroxide nanowire architectures with a superior volumetric capacitance for supercapacitors. *Advanced Functional Materials*, 25(14):2109-2116, 2015.

[10] Dong, M., Wang, Z., Yan, G., Wang, J., Guo, H. and Li, X. Confine growth of NiCo2S4 nanoneedles in graphene framework toward high-performance asymmetric capacitor. *Journal of Alloys and Compounds*, 822:153645, 2020.

[11] Shen, L., Wang, J., Xu, G., Li, H., Dou, H. and Zhang, X. NiCo2S4 nanosheets grown on nitrogen-doped carbon foams as an advanced electrode for supercapacitors. *Advanced Energy Materials*, 5(3):1400977, 2015.

[12] Chen, J., Xu, J., Zhou, S., Zhao, N. and Wong, C.-P. Nitrogen-doped hierarchically porous carbon foam: a free-standing electrode and mechanical support for high-performance supercapacitors. *Nano Energy*, 25:193-202, 2016.

[13] Fan, Y.-M., Liu, Y., Liu, X., Liu, Y. and Fan, L.-Z. Hierarchical porous NiCo2S4-rGO composites for high-performance supercapacitors. *Electrochimica Acta*, 249:1-8, 2017.

[14] Panicker, N. J. and Sahu, P. P. Green reduction of graphene oxide using phytochemicals extracted from Pomelo Grandis and Tamarindus indica and its supercapacitor applications. *Journal of Materials Science: Materials in Electronics*:1-14, 2021.

[15] Li, D., Müller, M. B., Gilje, S., Kaner, R. B. and Wallace, G. G. Processable aqueous dispersions of graphene nanosheets. *Nature nanotechnology*, 3(2):101-105, 2008.

[16] Cai, X., Shen, X., Ma, L. and Ji, Z. Facile synthesis of nickel–cobalt sulfide/reduced graphene oxide hybrid with enhanced capacitive performance. *RSC Advances,* 5(72):58777-58783, 2015.

[17] Alam, S. N., Sharma, N. and Kumar, L. Synthesis of graphene oxide (GO) by modified hummers method and its thermal reduction to obtain reduced graphene oxide (rGO). *Graphene,* 6(1):1-18, 2017.

[18] Li, B., Jin, X., Lin, J. and Chen, Z. Green reduction of graphene oxide by sugarcane bagasse extract and its application for the removal of cadmium in aqueous solution. *Journal of Cleaner Production*, 189:128-134, 2018.

[19] Phukan, P., Narzary, R. and Sahu, P. P. A green approach to fast synthesis of reduced graphene oxide using alcohol for tuning semiconductor property. *Materials Science in Semiconductor Processing,* 104:104670, 2019.

[20] Narzary, R., Phukan, P. and Sahu, P. P. Efficiency Enhancement of Low-Cost Heterojunction Solar Cell by the Incorporation of Highly Conducting rGO Into ZnO Nanostructure. *IEEE Transactions on Electron Devices*, 2021.

[21] Panicker, N. J., Ajayan, P. M. and Sahu, P. P. Band-gap tuned hexagonal-boron nitride/reduced graphene oxide superlattice wrapped cadmium sulfide/Polypyrrole nanocomposite as an efficient supercapacitor electrode material. *Journal of Energy Storage*, 56:105901, 2022.

[22] Kudin, K. N., Ozbas, B., Schniepp, H. C., Prud'Homme, R. K., Aksay, I. A. and Car, R. Raman spectra of graphite oxide and functionalized graphene sheets. *Nano letters*, 8(1):36-41, 2008.

[23] Zhang, Y., Li, P., Yin, X., Yan, Y., Zhan, K., Yang, J. and Zhao, B. Cobalt sulfide supported on nitrogen and sulfur dual-doped reduced graphene oxide for highly active oxygen reduction reaction. *RSC advances*, 7(79):50246-50253, 2017.

[24] Li, Z., Wang, X., Yin, Z., Zhao, J., Song, M., Wu, Z., Li, H. and Wang, X. Ag nanoparticles decorated N/S dual-doped graphene nanohybrids for high-performance asymmetric supercapacitors. *Carbon*, 161:726-735, 2020.

[25] Bandosz, T. J. and Ren, T.-Z. Porous carbon modified with sulfur in energy related applications. *Carbon*, 118:561-577, 2017.

[26] Panicker, N. J., Dutta, J. C. and Sahu, P. P. Confined growth of NiCo2S4 on 2D/2D porous carbon self-repairing g-C3N4/rGO heterostructure for enhanced performance of asymmetric supercapacitors. *Chemical Engineering Journal*:142376, 2023.

[27] Li, F., Li, Q., Kimura, H., Xie, X., Zhang, X., Wu, N., Sun, X., Xu, B. B., Algadi, H. and Pashameah, R. A. Morphology controllable urchin-shaped bimetallic nickel-cobalt oxide/carbon composites with enhanced electromagnetic wave absorption performance. *Journal of Materials Science & Technology*, 148:250-259, 2023.

[28] Mu, Q., Liu, R., Kimura, H., Li, J., Jiang, H., Zhang, X., Yu, Z., Sun, X., Algadi, H. and Guo, Z. Supramolecular self-assembly synthesis of hemoglobin-like amorphous CoP@ N, P-doped carbon composites enable ultralong stable cycling under high-current density for lithium-ion battery anodes. *Advanced Composites and Hybrid Materials*, 6(1):23, 2023.

[29] Jiang, L., Yao, M., Liu, B., Li, Q., Liu, R., Lv, H., Lu, S., Gong, C., Zou, B. and Cui, T. Controlled synthesis of CeO2/graphene nanocomposites with highly enhanced optical and catalytic properties. *The Journal of Physical Chemistry C*, 116(21):11741-11745, 2012.

[30] Zhu, Y., Wu, Z., Jing, M., Yang, X., Song, W. and Ji, X. Mesoporous NiCo2S4 nanoparticles as high-performance electrode materials for supercapacitors. *Journal of Power Sources*, 273:584-590, 2015.

[31] Wu, Z.-S., Ren, W., Gao, L., Zhao, J., Chen, Z., Liu, B., Tang, D., Yu, B., Jiang, C. and Cheng, H.-M. Synthesis of graphene sheets with high electrical conductivity and good thermal stability by hydrogen arc discharge exfoliation. *ACS nano*, 3(2):411-417, 2009.

[32] Jiang, Y. and Liu, J. Definitions of pseudocapacitive materials: a brief review. *Energy & Environmental Materials*, 2(1):30-37, 2019.

[33] Huang, Z.-H., Liu, T.-Y., Song, Y., Li, Y. and Liu, X.-X. Balancing the electrical double layer capacitance and pseudocapacitance of hetero-atom doped carbon. *Nanoscale*, 9(35):13119-13127, 2017.

[34] Chang, Y., Shi, H., Yan, X., Zhang, G. and Chen, L. A ternary B, N, P-Doped carbon material with suppressed water splitting activity for high-energy aqueous supercapacitors. *Carbon*, 170:127-136, 2020.

[35] Li, Z., Ji, X., Han, J., Hu, Y. and Guo, R. NiCo2S4 nanoparticles anchored on reduced graphene oxide sheets: in-situ synthesis and enhanced capacitive performance. *Journal of colloid and interface science*, 477:46-53, 2016.

[36] Hsiang, H.-I., She, C.-H. and Chung, S.-H. Materials and electrode designs of high-performance NiCo2S4/Reduced graphene oxide for supercapacitors. *Ceramics International*, 2021.

[37] Wu, Y., Yan, M., Sun, L. and Shi, W. Flexible yolk-shelled NiCo 2 S 4 hollow spheres/RGO film electrodes for efficient supercapacitive energy storage. *New Journal of Chemistry*, 42(19):16174-16182, 2018.

[38] Chhetri, K., Dahal, B., Mukhiya, T., Tiwari, A. P., Muthurasu, A., Kim, T., Kim, H. and Kim, H. Y. Integrated hybrid of graphitic carbon-encapsulated CuxO on multilayered mesoporous carbon from copper MOFs and polyaniline for asymmetric supercapacitor and oxygen reduction reactions. *Carbon*, 179:89-99, 2021.

[39] Peng, S., Li, L., Li, C., Tan, H., Cai, R., Yu, H., Mhaisalkar, S., Srinivasan, M., Ramakrishna, S. and Yan, Q. In situ growth of NiCo 2 S 4 nanosheets on graphene for high-performance supercapacitors. *Chemical communications*, 49(86):10178-10180, 2013.

[40] Mukhiya, T., Dahal, B., Ojha, G. P., Chhetri, K., Lee, M., Kim, T., Chae, S.-H., Tiwari, A. P., Muthurasu, A. and Kim, H. Y. Silver nanoparticles entrapped cobalt oxide nanohairs/electrospun carbon nanofibers nanocomposite in apt architecture for high performance supercapacitors. *Composites Part B: Engineering*, 178:107482, 2019.

[41] Sarmah, S., Kakati, B. K. and Deka, D. Recent advancement in rechargeable battery technologies. *Wiley Interdisciplinary Reviews: Energy and Environment*:e461.

[42] Das, J. and Sahu, P. P. Water splitting with screw pitched cylindrical electrode and Fe (OH) 2 catalyst under 1.4 V. *Renewable Energy*, 165:525-532, 2021.

[43] Vinoth, S., Subramani, K., Ong, W.-J., Sathish, M. and Pandikumar, A. CoS2 engulfed ultra-thin S-doped g-C3N4 and its enhanced electrochemical performance in hybrid asymmetric supercapacitor. *Journal of colloid and interface science*, 584:204-215, 2021.

[44] Yu, X. Y., Yu, L. and Lou, X. W. Metal sulfide hollow nanostructures for electrochemical energy storage. *Advanced Energy Materials*, 6(3):1501333, 2016.

[45] Guo, W., Wang, J., Fan, C., Chen, Z., Liu, P., Zhu, D., Xu, Z., Pang, L. and Li, T. Synthesis of carbon self-repairing porous g-C3N4 nanosheets/NiCo2S4 nanoparticles hybrid composite as high-performance electrode materials for supercapacitors. *Electrochimica Acta*, 253:68-77, 2017.

[46] Luo, Y., Yan, Y., Zheng, S., Xue, H. and Pang, H. Graphitic carbon nitride based materials for electrochemical energy storage. *Journal of materials chemistry A*, 7(3):901-924, 2019.

[47] Ashritha, M. and Hareesh, K. A review on Graphitic Carbon Nitride based binary nanocomposites as supercapacitors. *Journal of Energy Storage*, 32:101840, 2020.

[48] Ding, Y., Tang, Y., Yang, L., Zeng, Y., Yuan, J., Liu, T., Zhang, S., Liu, C. and Luo, S. Porous nitrogen-rich carbon materials from carbon self-repairing gC 3 N 4 assembled with graphene for high-performance supercapacitor. *Journal of materials chemistry A*, 4(37):14307-14315, 2016.

[49] Li, L., Qin, J., Bi, H., Gai, S., He, F., Gao, P., Dai, Y., Zhang, X., Yang, D. and Yang, P. Ni (OH) 2 nanosheets grown on porous hybrid g-C3N4/RGO network as high performance supercapacitor electrode. *Scientific reports*, 7(1):1-11, 2017.

[50] Chen, Q., Zhao, Y., Huang, X., Chen, N. and Qu, L. Three-dimensional graphitic carbon nitride functionalized graphene-based high-performance supercapacitors. *Journal of materials chemistry A*, 3(13):6761-6766, 2015.

[51] Lin, R., Li, Z., Abou El Amaiem, D. I., Zhang, B., Brett, D. J., He, G. and Parkin, I. P. A general method for boosting the supercapacitor performance of graphitic carbon nitride/graphene hybrids. *Journal of materials chemistry A*, 5(48):25545-25554, 2017.

[52] Cao, L., Tang, G., Mei, J. and Liu, H. Construct hierarchical electrode with NixCo3-xS4 nanosheet coated on NiCo2O4 nanowire arrays grown on carbon fiber paper for high-performance asymmetric supercapacitors. *Journal of Power Sources*, 359:262-269, 2017.

[53] Wang, Y., Chen, Z., Lei, T., Ai, Y., Peng, Z., Yan, X., Li, H., Zhang, J., Wang, Z. M. and Chueh, Y. L. Hollow NiCo2S4 Nanospheres Hybridized with 3D Hierarchical Porous rGO/Fe2O3 Composites toward High-Performance Energy Storage Device. *Advanced Energy Materials*, 8(16):1703453, 2018.

[54] Beka, L. G., Li, X., Wang, X., Han, C. and Liu, W. A hierarchical NiCo 2 S 4 honeycomb/NiCo 2 S 4 nanosheet core–shell structure for supercapacitor applications. *RSC advances*, 9(55):32338-32347, 2019.

[55] Ouyang, Y., Zhang, B., Wang, C., Xia, X., Lei, W. and Hao, Q. Bimetallic metal-organic framework derived porous NiCo2S4 nanosheets arrays as binder-free electrode for hybrid supercapacitor. *Applied Surface Science*, 542:148621, 2021.

[56] Liang, X., He, H., Yang, X., Lü, W., Wang, L. and Li, X. In-situ growth of bimetallic sulfide NiCo2S4 nanowire on carbon cloth for asymmetric flexible supercapacitors. *Journal of Energy Storage*, 42:103105, 2021.

[57] Yi, T.-F., Pan, J.-J., Wei, T.-T., Li, Y. and Cao, G. NiCo2S4-based nanocomposites for energy storage in supercapacitors and batteries. *Nano Today*, 33:100894, 2020.

[58] Moussa, M., El-Kady, M. F., Zhao, Z., Majewski, P. and Ma, J. Recent progress and performance evaluation for polyaniline/graphene nanocomposites as supercapacitor electrodes. *Nanotechnology*, 27(44):442001, 2016.

[59] Panicker, N. J. and Sahu, P. P. Green reduction of graphene oxide using phytochemicals extracted from Pomelo Grandis and Tamarindus indica and its supercapacitor applications. *Journal of Materials Science: Materials in Electronics*, 32(11):15265-15278, 2021.

[60] Ma, Y., Liu, E., Hu, X., Tang, C., Wan, J., Li, J. and Fan, J. A simple process to prepare few-layer g-C3N4 nanosheets with enhanced photocatalytic activities. *Applied Surface Science*, 358:246-251, 2015.

[61] Ong, W.-J., Tan, L.-L., Chai, S.-P., Yong, S.-T. and Mohamed, A. R. Surface charge modification via protonation of graphitic carbon nitride (g-C3N4) for electrostatic self-assembly construction of 2D/2D reduced graphene oxide (rGO)/g-C3N4 nanostructures toward enhanced photocatalytic reduction of carbon dioxide to methane. *Nano Energy*, 13:757-770, 2015.

[62] Zhang, J., Ding, J., Li, C., Li, B., Li, D., Liu, Z., Cai, Q., Zhang, J. and Liu, Y. Fabrication of novel ternary three-dimensional RuO2/graphitic-C3N4@ reduced graphene oxide aerogel composites for supercapacitors. *ACS Sustainable Chemistry & Engineering*, 5(6):4982-4991, 2017.

[63] Liu, T., Zhang, X., Li, B., Ding, J., Liu, Y., Li, G., Meng, X., Cai, Q. and Zhang, J. Fabrication of quasi-cubic Fe_3O_4@ rGO composite via a colloid electrostatic self-assembly process for supercapacitors. 2014.

[64] Liu, Y., Jiang, X., Li, B., Zhang, X., Liu, T., Yan, X., Ding, J., Cai, Q. and Zhang, J. Halloysite nanotubes@ reduced graphene oxide composite for removal of dyes from water and as supercapacitors. *Journal of materials chemistry A*, 2(12):4264-4269, 2014.

[65] Su, F. Y., Xu, C. Q., Yu, Y. X. and Zhang, W. D. Carbon Self-Doping Induced Activation of n–π* Electronic Transitions of g-C3N4 Nanosheets for Efficient Photocatalytic H2 Evolution. *ChemCatChem,* 8(22):3527-3535, 2016.

[66] Groenewolt, M. and Antonietti, M. Synthesis of g-C3N4 nanoparticles in mesoporous silica host matrices. *Advanced Materials,* 17(14):1789-1792, 2005.

[67] Cao, S., Low, J., Yu, J. and Jaroniec, M. Polymeric photocatalysts based on graphitic carbon nitride. *Advanced Materials,* 27(13):2150-2176, 2015.

[68] Narzary, R., Phukan, P. and Sahu, P. P. Efficiency Enhancement of Low-Cost Heterojunction Solar Cell by the Incorporation of Highly Conducting rGO Into ZnO Nanostructure. *IEEE Transactions on Electron Devices,* 68(7):3238-3245, 2021.

[69] Cheng, Y., Tay, B., Lau, S. P., Shi, X., Qiao, X., Chen, J., Wu, Y. and Xie, C. Raman spectroscopy of carbon nitride films deposited using the filtered cathodic vacuum-arc technique combined with a radio-frequency nitrogen-ion beam. *Applied physics A,* 73(3):341-345, 2001.

[70] Zhang, W., Huang, H., Li, F., Deng, K. and Wang, X. Palladium nanoparticles supported on graphitic carbon nitride-modified reduced graphene oxide as highly efficient catalysts for formic acid and methanol electrooxidation. *Journal of materials chemistry A,* 2(44):19084-19094, 2014.

[71] Liu, Z., Duan, X., Zhou, X., Qian, G., Zhou, J. and Yuan, W. Controlling and formation mechanism of oxygen-containing groups on graphite oxide. *Industrial & Engineering Chemistry Research,* 53(1):253-258, 2014.

[72] Zhao, W., Guo, Y., Wang, S., He, H., Sun, C. and Yang, S. A novel ternary plasmonic photocatalyst: ultrathin g-C3N4 nanosheet hybrided by Ag/AgVO3 nanoribbons with enhanced visible-light photocatalytic performance. *Applied Catalysis B: Environmental,* 165:335-343, 2015.

[73] Bao, N., Hu, X., Zhang, Q., Miao, X., Jie, X. and Zhou, S. Synthesis of porous carbon-doped g-C3N4 nanosheets with enhanced visible-light photocatalytic activity. *Applied Surface Science,* 403:682-690, 2017.

[74] Kim, M. S., Lim, E., Kim, S., Jo, C., Chun, J. and Lee, J. General Synthesis of N-Doped Macroporous Graphene-Encapsulated Mesoporous Metal Oxides and Their Application as New Anode Materials for Sodium-Ion Hybrid Supercapacitors. *Advanced Functional Materials,* 27(3):1603921, 2017.

[75] Bafaqeer, A., Tahir, M., Ali Khan, A. and Saidina Amin, N. A. Indirect Z-scheme assembly of 2D ZnV2O6/RGO/g-C3N4 nanosheets with RGO/pCN as solid-state electron

mediators toward visible-light-enhanced CO2 reduction. *Industrial & Engineering Chemistry Research,* 58(20):8612-8624, 2019.

[76] Hou, Y., Wen, Z., Cui, S., Guo, X. and Chen, J. Constructing 2D porous graphitic C3N4 nanosheets/nitrogen-doped graphene/layered MoS2 ternary nanojunction with enhanced photoelectrochemical activity. *Advanced Materials,* 25(43):6291-6297, 2013.

[77] Pawar, R. C., Khare, V. and Lee, C. S. Hybrid photocatalysts using graphitic carbon nitride/cadmium sulfide/reduced graphene oxide (gC 3 N 4/CdS/RGO) for superior photodegradation of organic pollutants under UV and visible light. *Dalton Transactions,* 43(33):12514-12527, 2014.

[78] McAllister, M. J., Li, J.-L., Adamson, D. H., Schniepp, H. C., Abdala, A. A., Liu, J., Herrera-Alonso, M., Milius, D. L., Car, R. and Prud'homme, R. K. Single sheet functionalized graphene by oxidation and thermal expansion of graphite. *Chemistry of materials,* 19(18):4396-4404, 2007.

[79] Kumar, S., Sekar, S., Kaliamurthy, A. K. and Lee, S. Bifunctional rGO-NiCo2S4 MOF hybrid with high electrochemical and catalytic activity for supercapacitor and nitroarene reduction. *Journal of Materials Research and Technology,* 12:2489-2501, 2021.

[80] Dong, M., Wang, Z., Li, X., Guo, H. and Wang, J. A smart architecture of nickel-cobalt sulfide nanotubes assembled nanoclusters for high-performance pseudocapacitor. *Journal of Alloys and Compounds,* 765:505-511, 2018.

[81] Wang, J.-G., Zhou, R., Jin, D., Xie, K. and Wei, B. Controlled synthesis of NiCo2S4 nanostructures on nickel foams for high-performance supercapacitors. *Energy Storage Materials,* 2:1-7, 2016.

[82] Ren, C., Jia, X., Zhang, W., Hou, D., Xia, Z., Huang, D., Hu, J., Chen, S. and Gao, S. Hierarchical porous integrated Co1− xS/CoFe2O4@ rGO nanoflowers fabricated via temperature-controlled in situ calcining sulfurization of multivariate CoFe-MOF-74@ rGO for high-performance supercapacitor. *Advanced Functional Materials,* 30(45):2004519, 2020.

[83] Sarkar, A., Singh, A. K., Sarkar, D., Khan, G. G. and Mandal, K. Three-dimensional nanoarchitecture of BiFeO3 anchored TiO2 nanotube arrays for electrochemical energy storage and solar energy conversion. *ACS Sustainable Chemistry & Engineering,* 3(9):2254-2263, 2015.

[84] Wu, Q., He, T., Zhang, Y., Zhang, J., Wang, Z., Liu, Y., Zhao, L., Wu, Y. and Ran, F. Cyclic stability of supercapacitors: materials, energy storage mechanism, test methods, and device. *Journal of materials chemistry A,* 2021.

[85] Cui, Y., Zhang, J., Li, G., Sun, Y., Zhang, G. and Zheng, W. Ionic liquid-assisted synthesis of rGO wrapped three-dimensional CuS ordered nanoerythrocytes with enhanced performance for asymmetric supercapacitors. *Chemical Engineering Journal*, 325:424-432, 2017.

[86] Wang, K., Yan, R., Tian, X., Wang, Y., Lei, S., Li, X., Yang, T., Wang, X., Song, Y. and Liu, Y. Multi-scale biomass-based carbon microtubes decorated with Ni-Co sulphides nanoparticles for supercapacitors with high rate performance. *Electrochimica Acta*, 302:78-91, 2019.

[87] Cao, W., Liu, Y., Xu, F., Xia, Q., Du, G., Fan, Z. and Chen, N. Metal-organic framework derived carbon-coated spherical bimetallic nickel-cobalt sulfide nanoparticles for hybrid supercapacitors. *Electrochimica Acta*, 385:138433, 2021.

[88] Li, Z., Wu, L., Wang, L., Gu, A. and Zhou, Q. Nickel cobalt sulfide nanosheets uniformly anchored on porous graphitic carbon nitride for supercapacitors with high cycling performance. *Electrochimica Acta*, 231:617-625, 2017.

[89] Hou, Z.-Q., Yue, H.-P., Qi, Y.-C., Gao, Y.-P., Jia, X.-L., Yang, Z.-G., Liu, N.-N. and Huang, K.-J. NiCo2S4 nanoparticles grown on reduced graphene oxides for high-performance asymmetric supercapacitors. *Advanced Powder Technology*, 31(4):1603-1611, 2020.

[90] Zhao, F., Xie, D., Huang, W., Song, X., Sial, M. A. Z. G., Wu, H., Deng, F., Zhang, Q., Zou, J. and Zeng, X. Defect-rich honeycomb-like nickel cobalt sulfides on graphene through rapid microwave-induced synthesis for ultrahigh rate supercapacitors. *Journal of colloid and interface science*, 580:160-170, 2020.